The host galaxy and late-time evolution of the superluminous supernova PTF12dam

Monthly Notices
of the
ROYAL ASTRONOMICAL SOCIETY

MNRAS **452,** 1567–1586 (2015) doi:10.1093/mnras/stv1360

The host galaxy and late-time evolution of the superluminous supernova PTF12dam

T.-W. Chen,[1⋆] S. J. Smartt,[1⋆] A. Jerkstrand,[1⋆] M. Nicholl,[1] F. Bresolin,[2] R. Kotak,[1] J. Polshaw,[1] A. Rest,[3] R. Kudritzki,[2] Z. Zheng,[4] N. Elias-Rosa,[5,6] K. Smith,[1] C. Inserra,[1] D. Wright,[1] E. Kankare,[1,7] T. Kangas[8] and M. Fraser[9]

[1]*Astrophysics Research Centre, School of Maths and Physics, Queen's University Belfast, Belfast BT7 1NN, UK*
[2]*Institute for Astronomy, 2680 Woodlawn Drive, Honolulu, HI 96822, USA*
[3]*Space Telescope Science Institute, 3700 San Martin Dr., Baltimore, MD 21218, USA*
[4]*National Astronomical Observatories, Chinese Academy of Sciences, Beijing 100012, China*
[5]*INAF-Osservatorio Astronomico di Padova, Vicolo dell'Osservatorio 5, I-35122 Padova, Italy*
[6]*Institut de Ci'encies de lEspai (CSIC-IEEC), Campus UAB, Torre C5, 2a planta, E-08193 Barcelona, Spain*
[7]*Finnish Centre for Astronomy with ESO (FINCA), University of Turku, Väisäläntie 20, FI-21500 Piikkiö, Finland*
[8]*Tuorla Observatory, Department of Physics and Astronomy, University of Turku, Väisäläntie 20, FI-21500 Piikkiö, Finland*
[9]*Institute of Astronomy, University of Cambridge, Madingley Road, Cambridge CB3 0HA, UK*

Accepted 2015 June 17. Received 2015 June 10; in original form 2014 September 26

ABSTRACT

Superluminous supernovae (SLSNe) of Type Ic have a tendency to occur in faint host galaxies which are likely to have low mass and low metallicity. PTF12dam is one of the closest and best-studied superluminous explosions that has a broad and slowly fading light curve similar to SN 2007bi. Here we present new photometry and spectroscopy for PTF12dam from 200–500 d (rest frame) after peak and a detailed analysis of the host galaxy (SDSS J142446.21+461348.6 at $z = 0.107$). Using deep templates and image subtraction we show that the light curve can be fit with a magnetar model if escape of high-energy gamma rays is taken into account. The full bolometric light curve from −53 to +399 d (with respect to peak) cannot be fit satisfactorily with the pair-instability models. An alternative model of interaction with a dense circumstellar material (CSM) produces a good fit to the data although this requires a very large mass (∼13 $M_\odot$) of hydrogen-free CSM. The host galaxy is a compact dwarf (physical size ∼1.9 kpc) and with $M_g = -19.33 \pm 0.10$, it is the brightest nearby SLSN Ic host discovered so far. The host is a low-mass system (2.8×10^8 $M_\odot$) with a star formation rate (5.0 $M_\odot$ yr^{-1}), which implies a very high specific star formation rate (17.9 Gyr^{-1}). The remarkably strong nebular emission provide detections of the [O III] λ4363 and [O II] λλ7320, 7330auroral lines and an accurate oxygen abundance of $12 + \log(\mathrm{O/H}) = 8.05 \pm 0.09$. We show here that they are at the extreme end of the metallicity distribution of dwarf galaxies and propose that low metallicity is a requirement to produce these rare and peculiar SNe.

Key words: supernovae: general – supernovae: individual: PTF12dam – galaxies: abundances – galaxies: dwarf.

1 INTRODUCTION

New types of violent explosion labelled superluminous supernovae (SLSNe) have been discovered by the current generation of wide-field optical surveys. These SLSNe are 10–100 times brighter than normal core-collapse SNe (CCSNe) and reach absolute magnitudes above $M < -21$ (for a review, see Gal-Yam 2012). They have attracted considerable attention due to their potential utility as cosmological standard candles (see Inserra & Smartt 2014, for the first result on a standardization). However, the mechanism which powers such luminosities is still not well established. Some of these SLSNe show signs of strong interaction between high-velocity ejecta from a SN explosion and pre-existing dense circumstellar material. In such cases prominent lines of hydrogen are seen with multiple velocity components (e.g. Smith & McCray 2007; Smith et al. 2008; Benetti et al. 2014) and the source of the high and long-lasting luminosity is almost certainly reprocessing of the kinetic energy of the ejecta during collisions with slower moving shells. Another group

⋆ E-mail: tchen09@qub.ac.uk (T-WC); s.smartt@qub.ac.uk (SJS); a.jerkstrand@qub.ac.uk (AJ)

of SLSNe have been called SLSNe I or SLSNe Ic (we will use the latter term in this paper), since they do not generally exhibit hydrogen or helium lines in their optical spectra, and show no spectral signatures of interaction (e.g. Pastorello et al. 2010; Chomiuk et al. 2011; Quimby et al. 2011; Inserra et al. 2013). The first of these to be discovered was SN 2005ap (Quimby et al. 2007) which, when linked to the early Palomar Transient Factory (PTF) discoveries by Quimby et al. (2011), defined the class of these remarkable explosions. Some physical causes of the luminosity have been proposed. One is a model of spinning down magnetic neutron stars (Kasen & Bildsten 2010; Woosley 2010) and quantitative fits to some of these show good agreement (Chomiuk et al. 2011; Inserra et al. 2013). However, there are alternatives and the interaction model for these hydrogen-poor events is still plausible even though there are no obvious spectral signatures (Chevalier & Irwin 2011).

A few of these SLSNe Ic have light curves that decay quite slowly and the prototype of the class is SN 2007bi (Gal-Yam et al. 2009; Young et al. 2010). Gal-Yam et al. (2009) proposed that SN 2007bi was the result of a pair-instability supernova (PISN) explosion and the slowly fading light curve is driven by the decay of a large mass of ^{56}Ni in the ejecta. PTF10mnm is also a probable PISN candidate, and its light-curve shape and peak luminosity were fitted well with a massive PISN model from Kozyreva et al. (2014). However, other works, e.g. Nicholl et al. (2013) and McCrum et al. (2014), have recently shown that two SLSNe Ic (PTF12dam and PS1-11ap) have very similar observational characteristics to SN 2007bi, presenting better data before and around peak. They argue that the detailed light-curve fits to both the rise time and decay time cannot match the models of pair instability and that ^{56}Ni is not the cause of the extreme luminosity. Nicholl et al. (2013) and McCrum et al. (2014) argued that the observational data of both of these SLSNe Ic could be better explained by magnetar powering. The key point supporting magnetar engines rather than pair-instability explosions, is that the pre-maxima data show a steep rise that is not consistent with pair-instability models, but are well fit by magnetar models with 10–16 $M_\odot$ ejecta. This suggests that SN 2007bi may also not actually be a pair-instability explosion. This view was also expressed by the quantitative modelling of Kasen & Bildsten (2010) and Dessart et al. (2012) who both suggested a magnetar as an alternative power source to a large mass of radioactive ^{56}Ni. Another mechanism for boosting the luminosity of normal SNe is accretion on to compact remnants as recently suggested by Dexter & Kasen (2013).

All of these alternative models [magnetars, circumstellar material (CSM) interaction, radioactivity, accretion] to interpret SLSNe Ic have some success in reproducing the data sets currently available. Due to the relatively low volumetric rate of SLSNe Ic (e.g. Quimby et al. 2013; McCrum et al. 2014), the closest events have been found at redshifts between 0.1 and 0.3, and the observational data sets typically cover the evolution of the SNe in the ultraviolet (UV), optical and near-infrared (NIR) from around 30 d before peak to 100–200 d afterwards (rest frame). Distinguishing between models would benefit from wider wavelength coverage (e.g. in the X-rays as shown by Metzger et al. 2014) or observing SNe very late in their evolution. Gal-Yam et al. (2009) showed how the nebular spectrum of SN 2007bi (at +470 d) could be used to support a pair-instability interpretation. Nicholl et al. (2013) argued that while this was a consistent argument, one could also model the observed line flux with a much lower ejecta mass than that required for pair instability. Chen et al. (2013) illustrated the use of deep imaging at late times to set limits on the amount of ^{56}Ni explosively produced in SLSNe. An upper limit of ^{56}Ni mass ≤ 0.4 $M_\odot$ was found for SN 2010gx (Pastorello et al. 2010; Quimby et al. 2011) at 240–560 d after explosion. The studies of Inserra et al. (2013) and Nicholl et al. (2014) further attempted to recover the fading stages of SLSNe Ic and fit the luminosity with the magnetar model.

SLSNe Ic appear to have a preference for occurring in faint, dwarf galaxies (Neill et al. 2011), and they also show a trend towards low-metallicity environment (Stoll et al. 2011; Chen et al. 2013; Lunnan et al. 2013). The most reliable method to quantitatively determine oxygen abundance without calibration uncertainties is the 'direct method' which requires the electron temperature T_e to be estimated from the auroral [O III] λ4363 line. The first detailed study of an SLSN Ic host (SN 2010gx) using the detection of this line (Chen et al. 2013) suggested that low metallicity plays a critical role in producing SLSNe Ic. They found the host of SN 2010gx to have the lowest metallicity of any SN to date; the oxygen abundance of $12 + \log(\mathrm{O/H}) = 7.4 \pm 0.1$ (employing the direct T_e method) is equivalent to 0.05 $Z_\odot$ for a solar value of $12 + \log(\mathrm{O/H}) = 8.69 \pm 0.05$ (Asplund et al. 2009). Lunnan et al. (2013) found the metallicity of the host of PS1-10bzj to be $12 + \log(\mathrm{O/H}) = 7.8 \pm 0.2$ (also using the T_e method with a detection of the weak [O III] 4364 line). This host has the highest specific star formation rate (sSFR) $\sim$100 Gyr^{-1} among all SLSN Ic hosts so far. The stellar mass of the hosts of SLSNe Ic tend to fall below 10^9 $M_\odot$, hence their sSFR are quite high even for dwarf galaxies in the local Universe (Chen et al. 2013; Lunnan et al. 2014).

Low metallicity may be a major constraint on the progenitor channel of SLSNe Ic, if it is a common and exclusive feature among the dwarf galaxy hosts. However the auroral [O III] λ4363 line is often weak and at redshifts between 0.1 and 0.5 are difficult to detect. Spectroscopy with 10 m-class telescopes is needed and even then the emission line strengths of the hosts vary considerably such that the detection of this line is not always possible. The more commonly used metallicity diagnostic is the R_{23} strong line method, based on the ratio of [O III] $\lambda\lambda$4959, 5007/Hβ. The majority of estimates of metallicity for the sites of SLSNe Ic to date (Young et al. 2010; Lunnan et al. 2014; McCrum et al. 2014) are from measuring the strong nebular line Hβ, and the forbidden [O III] /[O II] lines and applying a calibration such as McGaugh (1991, hereafter M91). However it has been known for some time that the calibration of the strong line methods vary by nearly an order of magnitude. Typically there are systematic offsets of 0.2–0.4 dex (and sometimes up to 0.6 dex) between the R_{23} calibration and abundances determined on an electron temperature scale (Liang et al. 2007; Bresolin 2011). An additional complication for the R_{23} calibration is that there are two branches of the calibration curve and one needs to know which one to apply. Hence it is desirable, where possible, to measure the strength of the weak [O III] λ4363 line. The most extensive study to date of SLSN Ic hosts is by Lunnan et al. (2014) who found that 31 hosts are in general low mass ($\sim 10^8$ $M_\odot$), low luminosity and low metallicity ($\sim$0.45 $Z_\odot$) based on R_{23} method, and have a high median sSFR ($\sim$2 Gyr^{-1}). They suggested the SLSN Ic host population is similar to long gamma-ray burst (LGRB) hosts. Recently, Leloudas et al. (2015) suggested that, while the host galaxies are similar for SLSNe Ic and LGRBs, SLSN hosts are in fact more extreme. They found that half of their sample of SLSN Ic hosts are extreme emission line galaxies [EELGs; having emission lines with equivalent width (EW) > 100 Å], and claimed that the progenitors of SLSNe Ic are the first generation of stars to explode in a starburst – even younger than GRBs. In contrast, Lunnan et al. (2015) found that the locations of SLSNe within their hosts do trace the UV light, and thus are correlated with recent star formation (massive progenitors), but they appear to have less of a preference for occurring in the brightest regions than do LGRBs (e.g. Kelly et al. 2014). Hence

they suggested that SLSN Ic progenitors are older/less massive stars than those of LGRBs.

As PTF12dam is one of the closest SLSNe Ic ever found at redshift $z = 0.107$, this provides an opportunity to study a host galaxy in detail. This galaxy has exceptionally strong emission lines and with auroral lines of three atomic species available one can determine abundances more precisely than done before. In this paper we present imaging and spectroscopy data at very late epochs in the SN evolution; the multiwavelength light-curves sample out to 400 d (rest frame) after peak and nebular spectra are presented at ∼500 d. A major complication with this observational experiment is that SLSNe Ic are usually found in faint, but compact, host galaxies and hence distinguishing between SN flux and galaxy flux requires careful long-term monitoring. The host galaxies and explosion environments are themselves of interest and a study of the late-time evolution is necessarily aligned with quantifying the host galaxy contribution. The requirement to separate host galaxy flux from SN flux necessitates a careful joint analysis of these two flux.

Since PTF12dam has a slowly fading light curve like SN 2007bi and PS1-11ap, we also compared these three SN host galaxies. The paper is organized as follows: in Section 2, we detail the photometric follow-up and spectroscopic observations of PTF12dam and its host galaxy. We also present new photometric data of the host of SN 2007bi. Section 3 discusses the various host galaxy properties, the methods to determinate the host stellar mass, metallicity and SFR, etc. Section 4 investigates the bolometric light curve of PTF12dam from −52 to +399 d. Our discussion on light-curve modelling is presented in Section 5, and on the host in Section 6. Finally, we conclude in Section 7.

2 OBSERVATIONAL DATA AND ANALYSIS

2.1 Host galaxy photometry

The host of PTF12dam is a clear source detected in the Sloan Digital Sky Survey (SDSS) images (SDSS J142446.21+461348.6) taken on 2003 February 11, about 10 yr before the explosion of PTF12dam. While we have gathered deeper and higher resolution images of PTF12dam and its host at ∼ 2 yr after the SN explosion, we used the SDSS magnitudes as the most appropriate for the host galaxy since they unambiguously do not contain any SN light. We adopted the apparent Petrosian AB magnitudes $u = 19.79 \pm 0.05$, $g = 19.36 \pm 0.02$, $r = 19.20 \pm 0.02$, $i = 18.83 \pm 0.03$ and $z = 19.32 \pm 0.14$ from the SDSS version 9 data release catalogue (DR9; Ahn et al. 2012) for the PTF12dam host galaxy. The host is also detected in the *Galaxy Evolution Explorer* (*GALEX*) images, having the UV magnitudes of FUV = 20.13 ± 0.19 (∼1528 Å) and NUV = 20.13 ± 0.14 (∼2271 Å) in the AB system (GR6 catalogue[1]), which corresponds to the object GALEX J142446.2+461348.

The host galaxy of PTF12dam is not detected in the Two Micron All Sky Survey (2MASS), its brightness is below the sensitivity limits of $J = 17.0$, $H = 16.0$, $K = 15.5$ (see supplementary information in Nicholl et al. 2013) and also is not detected in the available *Wide-field Infrared Survey Explorer* (limit 17.23 mag at 3.4 μm; Wright et al. 2010) or *Spitzer Space Telescope* images. Hence we lack any NIR pre-SN constraints on the host. However, we obtained deep JHK_s images with the 2.6-m Nordic Optical Telescope (NOT) on 2014 February 13, which was +554 d past peak (rest frame). The NIR camera on NOT, NOTCam, is a 1024 × 1024 pixel array providing a field of view of 4 arcmin × 4 arcmin with 0.23 arcsec pixels. Those images were reduced by the external IRAF/NOTCAM package which applies flat-fielding and sky background subtractions. Aperture photometry within the IRAF/DAOPHOT package was carried out using an aperture of ∼3 arcsec, which encompassed the whole galaxy. We used the same aperture size to measure the flux of two 2MASS reference stars in the field to set the zero-point in each band. To ensure better relative photometry amongst the other epoch measurements, we added three other stars which were detected in the NOT images as local secondary standards. This led to derived NIR magnitudes of the host of PTF12dam of $J = 18.37 \pm 0.15$, $H = 17.82 \pm 0.13$ and $K_s = 17.16 \pm 0.09$ in the Vega system. We assumed that the detected flux in the NOT NIR images is exclusively host galaxy, with negligible contribution from the SN flux. As discussed below, the measured *J*-band flux of PTF12dam (with image subtraction) is almost 2 mag fainter than the host at +342 d after peak and at a decline rate of roughly 1 mag per 100 d, we would expect it to be ∼4 mag fainter than the measured host flux at this epoch of +553 d (and even fainter in *H* and K_s; see Table 3).

Additionally, as PTF12dam is similar to SN 2007bi (Nicholl et al. 2013), we have pursued further investigation of the host of SN 2007bi (SDSS J131920.14+085543.7). The SDSS detection published in Young et al. (2010) is marginal in *g* and *r* and there are no flux detections in the other bands. Young et al. (2010) published estimates of the late-time photometry of SN 2007bi and its host galaxy from the ESO 8-m Very Large Telescope and the 2-m Liverpool Telescope (LT; Steele et al. 2004). However disentangling the host from the SN flux was still not unambiguous. Therefore, we took deep images on the 4.2-m William Herschel Telescope (WHT) with the auxiliary-port camera (ACAM) instrument on 2012 May 25. This camera provides imaging over 8 arcmin (0.25 arcsec per pixel) with a low fringing deep depleted 2k × 4k EEV CCD. Images were taken through the *griz* filters on ACAM, (specifically filters 701 SlnG, 702 SlnR, 703 SlnI, 704 SlnZ). These were reduced in standard fashion by debiasing and flat-fielding with twilight sky frames. Zero-points were determined with 10 SDSS reference stars in the field, and aperture photometry was carried out within IRAF/DAOPHOT using an aperture of ∼2.3 arcsec to cover the whole galaxy. We estimated apparent AB magnitudes $g = 22.84 \pm 0.10$, $r = 22.36 \pm 0.08$, $i = 22.23 \pm 0.09$ and $z = 21.98 \pm 0.13$ for the host of SN 2007bi. Colour images of each are shown in Fig. 1.

2.2 Host galaxy spectroscopy

A large number of spectra of PTF12dam have been presented in Nicholl et al. (2013) showing the very strong emission line nature of SDSS J142446.21+461348.6. We took additional spectra of PTF12dam since that paper was submitted and the main data we will focus on here for host galaxy analysis were taken on 2013 March 30. At this date, the SN was +265 d after peak (rest frame). The spectrum was taken with the WHT + Intermediate dispersion Spectrograph and Imaging System (ISIS), listed in Table 1. The dichroic was removed and the spectra were taken in the red and blue arms separately, since the Hβ line at $z = 0.107$ falls almost right on the dichroic crossover point, leading to uncertain flux calibration. In the red arm, the R158R grating was used (dispersion = 1.8 Å pixel^{-1}) with an order-blocking filter GG495 and central wavelength of 7500 Å, giving coverage 5075–9170 Å. We used a 1.0 arcsec slit to obtain three spectra of 1800 s exposures each. The object position was shifted by ∼10 pixels along the slit for

[1] http://galex.stsci.edu/GR6/

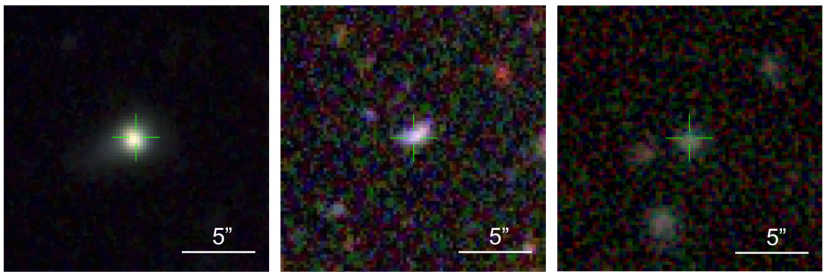

Figure 1. RGB-colour-combined host galaxy images. The SN position is marked with green crosshairs and was determined by superimposing the SN image at peak brightness to the host galaxy frame (Young et al. 2010; Nicholl et al. 2013; McCrum et al. 2014). The images are 20 arcsec × 20 arcsec with north pointing up and east to the left. Left: the host of PTF12dam combined with *gri*-band images. Central: the host of SN 2007bi combined with *gri*-band images. Right: the host of PS1-11ap combined with Pan-STARRS1 $r_{\rm P1}i_{\rm P1}z_{\rm P1}$ filter images.

Table 1. Log of spectroscopic observations of PTF12dam and its host galaxy used in this paper. The WHT spectrum at −13.6 d, and the TNG spectrum, are from Nicholl et al. (2013). The resolution was estimated from the FWHM of sky lines.

Date	MJD	Phase (d)	Telescope	Instrument + Grism/Grating	Exposure (s)	Slit (arcsec)	Resolution (Å)	Range (Å)
2012 May 25	56072.91	−13.6	WHT	ISIS + R300B	900	0.7	3	3000–5400
2012 Jul 09	56117.99	27.1	TNG	NICS + IJ	600 × 6	1.5	35	8700–13 500
2013 Mar 30	56382.07	265.6	WHT	ISIS + R300B + R158R	1800 × 3	1	4, 6	3200–9170
2013 Mar 30	56382.09	265.6	WHT	ISIS + R300B + R158R	600	10	–	3200–9170
2013 Dec 25	56651.20	508.8	GTC	OSIRIS + R500R	2400 × 3	1	16	4900–9200

each individual frame, allowing us to remove the sky emission lines by two-dimensional image subtraction. The grating R300B (dispersion = 0.86 Å pixel^{-1}) was used for the blue arm with a central wavelength 4500 Å to cover 3200–5985 Å, and again a 1.0 arcsec slit was used and three 1800 s exposures taken. All observations were taken at the parallactic angle. To ensure that the spectra could be corrected for any slit losses, we took additional spectra with a 10.0 arcsec slit in both red and blue arms for covering the total flux of the galaxy (FWHM ∼ 1.5 arcsec). The exposure times of these spectra were 600 s each. In order to calibrate the flux carefully, we took two spectrophotometric standards, HZ44 and Feige 66, before and after the host observations, again with both the 1.0 and 10.0 arcsec slits. The wavelength calibrations were achieved using daytime CuNe+CuAr arcs. Detrending of the data, such as bias subtraction, and lamp flat-fielding was achieved using standard techniques within IRAF.

The combined blue and red spectra provide spectral coverage between 3200 and 9170 Å (rest-frame 2891–8284 Å) and the overlap region was used to ensure a uniform flux calibration, employing the three strong lines [O III] λ5007, [O III] λ4959 and Hβ. We measured the line flux in the red and blue arm spectra and applied a linear scaling (a scaling of 1.39 for red arm; 1.24 for blue arm) to bring both the 1.0-arcsec slit spectra into agreement with the 10.0-arcsec slit spectra. The line flux measured in the separate blue and red arms of these three lines agreed to within 1 per cent after this rescaling. Fig. 2 shows the final combined spectrum of the host galaxy. Although the spectrum contains flux from PTF12dam, the strength of the emission lines are secure given their strength and the fact that we subtract off the continuum. A wealth of emission lines were detected in the host. These include the auroral [O III] λ4363 line, which is essential for the most reliable metallicity calibration by estimating the electron temperature of the ionized gas from the flux ratio with [O III] λλ4959, 5007. The auroral [O II] doublet λλ7320,7330 was also a strong detection. The abundance analysis of these spectra is discussed in Section 3.4.

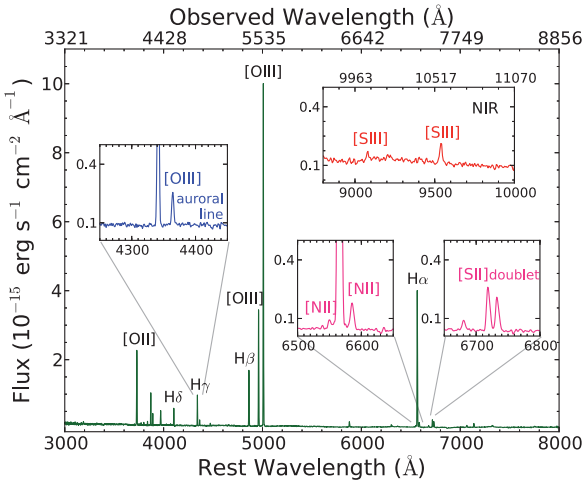

Figure 2. Spectrum of the host galaxy of PTF12dam. The [O III] λ4363 auroral line and the region near Hα are amplified. The NIR spectrum taken from Nicholl et al. (2013) is shown in the upper-right panel.

Line flux measurements were made after fitting a polynomial function to the continuum and subtracting off this contribution. This continuum flux is composed of the host galaxy continuum from its constituent stellar population and the SN flux from PTF12dam which is still visible. We fitted Gaussian line profiles using the QUB custom built PROCSPEC environment within IDL. The full width at half-maximum (FWHM) was allowed to vary for the Gaussian fits for the strong lines (defined as their EW ≥ 10 Å) and the unresolved blends; while we fixed the FWHM of single, weak lines (those with EW < 10 Å). The resolutions for the R300B and R158R gratings, for a 1.0 arcsec slit are similar ($R \simeq 1200$ and 1000, respectively) and we measured the arc lines to have FWHM = 3.7 Å in the blue and FWHM = 6.6 Å in the red. The single transition lines are marginally resolved. For the weak lines (EW <10 Å), we estimated

the average velocity from the three strongest lines ([O III] λ5007, [O III] λ4959 and Hβ) and then determined the appropriate FWHM to fix at the observed central wavelength of each. In addition, we fixed the widths of both [N II] λλ6548, 6583 lines in order to more reliably measure their flux and to discriminate from the wings of the nearby strong Hα line (even though the 6583 Å line was stronger than 10 Å). We did not fix the FWHM of the weak but clearly blended lines such as the [Fe III] λ4658 doublet and we also accepted the best-fitting FWHM for the strong [O II] λ3727 line, as it is has two unsolved components separated in wavelength by 2.8 Å.

We further normalized the spectrum and determined EW of all the identified lines. Uncertainties were estimated from the EW and rms of the continuum according to the equation from Gonzalez-Delgado et al. (1994):

$$\sigma_i = \sigma_c \sqrt{N + \frac{W_i}{\Delta}}, \quad (1)$$

where σ_i is the error of the flux of the emission line, σ_c is the rms measured from the local continuum, N is the measured line profile width in pixels, W_i is the absolute value of the line EW in Å, and Δ is the spectral dispersion in Å pixel^{-1}. The observed flux measurements and the related parameters are listed in Table 2, without any reddening corrections. The identified emission lines are those commonly seen in emission line galaxies, such as Green Peas (GPs; Amorín et al. 2012).

The [S III] lines listed at the bottom of Table 2 were measured from the NIR spectrum which was taken on 2012 July 9 with the Telescopio Nazionale Galileo (TNG) + Near Infrared Camera Spectrometer (NICS) and previously presented in (Nicholl et al. 2013, see Fig. 2). We fixed the width of FWHM of [S III] λ9069 line as the same velocity of [S III] λ9532. The flux ratio of λλ9532/9069 is ∼2.85. This is slightly different to the theoretical value of 2.44 expected in H II regions (Mendoza & Zeippen 1982). However given the weakness of the features, the strong continuum and uncertainty in its placement, and the telluric absorption located around the [S III] wavelength range this ratio is reasonably consistent with the theoretical one. There was no rescaling applied to match the NIR and the optical spectra due to no overlap in between.

Finally, we measured the host interstellar medium (ISM) absorption of the Mg II λλ2796/2803 doublet in the WHT spectrum of 2012 May 25 at the SN phase: −13.6 d from the peak (Nicholl et al. 2013). The rest-frame EWs are 2.11 ± 0.27 and 2.01 ± 0.28 Å, respectively, giving a ratio $W_{2796}/W_{2803} = 1.05$. See Section 3.4 for further discussion of these values.

2.3 Late-time monitoring of SLSN PTF12dam

The rise time of the early phase light curves presented in Nicholl et al. (2013) suggested that pair-instability models could not consistently fit the data. The light curves were better fit with simple magnetar engine models. However, continuous photometric follow-up to as late times as possible is essential to test this conclusion. To monitor the flux of PTF12dam beyond the time-scales presented in Nicholl et al. (2013), we imaged the source in optical and NIR filters on multiple epochs from +230 to +550 d, and additionally gathered a SN spectrum at +509 d after peak (rest frame) with the 10.4-m Gran Telescopio CANARIAS (GTC). Although this spectrum was taken much later than the WHT + ISIS spectrum it was not suitable for a metallicity analysis as it has much lower resolution, narrower wavelength coverage and the absolute flux calibration was not based on such careful observing procedures as employed at the WHT. All the spectroscopic data used in this paper are summarized in Table 1. The log of photometric observations is in Table 3. We defined the epoch of zero days as the date of *r*-band maximum on 2012 June 10 (MJD = 56088), rather than referring to the estimated date of SN explosion (MJD = 56017) from the magnetar model fit (Nicholl et al. 2013). All phases quoted here have been corrected for cosmological time dilation using the observed redshift $z = 0.107$ and are thus in the rest frame with respect to this peak magnitude date.

2.3.1 *Late-time photometric evolution of PTF12dam*

To cover the NIR (JHK_s bands), four epochs were taken by the NOT + NOTCam between +230 and +342 d (for details of NOTCam, see Section 2.1). We obtained deep images at phase +554 d which we assumed contained host galaxy flux only and negligible SN flux (as discussed in Section 2.1). These images were used as templates and subtracted from the four previous epochs. To do this, we aligned the images using the GEOMAP and GEOTRAN tasks within IRAF package and employed the image subtraction package, High Order Transform of PSF ANd Template Subtraction (HOTPANTS).[2] The FWHM of the point spread function (PSF) of the SN flux in these difference images was compared with the FWHM of surrounding stars. We found it to have similar values indicating that we were recovering a point-like source.

Magnitude measurements of the SN were carried out using aperture photometry with the IRAF/DAOPHOT task. We let the aperture size vary until we were confident that it encompassed the whole SN flux but avoided any negative pixels appearing in some subtraction images. The zero-point was set as discussed in Section 2.1. The SN magnitudes in these four epochs are listed in Table 3. In cases where the SN was undetected, we determined a 3σ limiting magnitude. We added 10 fake stars, of varying magnitude, within 1 arcmin radius around the SN position. We measured their magnitudes and uncertainties and then determined the 3σ detection limit to be when the standard deviation of the photometry of these fake stars was 0.3 mag. These detection limits are listed in Table 3. For consistency, we double checked that the detected SN magnitudes were brighter than the estimated detection limit of each frame.

The optical frames (*gri* bands) were taken with two different instrumental configurations: four epochs between +247 and +312 d from the LT + RATCam, and two later epochs (after +329 d) from the WHT + ACAM. We also took deep host images after +530 d using the same instruments to use as host galaxy templates and the observation log for these data is listed in Table 3. We assumed the LT images at +534 d and the WHT images at +550 d were dominated by the host galaxy flux and could be used as pure host templates. Although we can detect some broad emission line flux from PTF12dam in the +509 d spectrum (see Section 2.3.2), the overall SN flux in the broad-band filters was negligible. For example, in the *i* band, the SN flux is less than ∼1 per cent of the host flux ($i_{SN} \sim 25$ compared with $i_{host} \sim 19$).

The RATCam camera consists of a 2048 × 2048 EEV CCD giving a field of view of 4.6 arcmin and 0.135 arcsec per pixel sampling. This camera was formally decommissioned in 2014 February and we gathered images of PTF12dam (four epochs) and host template images through the filters *gri* before this replacement. The images were processed through the standard LT data reduction pipeline (bias-subtracted and flat-fielded). As with the NIR data, we aligned the images first using IRAF/GEOMAP and IRAF/GEOTRAN tasks,

[2] http://www.astro.washington.edu/users/becker/v2.0/hotpants.html

Table 2. Observed emission lines of the host of PTF12dam. The main optical spectrum was taken from the WHT on 2013 March 30. The lines highlighted in bold have been used to calculate the elemental abundances. We measured the Gaussian line profiles within the PROCSPEC task for strong lines (EW $\geq$ 10 Å), and fixed the FWHM for weak lines (EW $<$ 10 Å) in principle, except some lines marked with a $*$ symbol (see details in the Section 2.2). We measured [S III] λ9069 and λ9532 lines from the NIR spectrum taken on 2012 July 09 with the TNG + NICS (Nicholl et al. 2013). However, there is no overlap wavelength region between the main optical and NIR spectra. Hence there is no rescaling process for the NIR spectrum. The luminosity was derived from line flux, considering the luminosity distance of 481.1 Mpc, without any reddening correction.

Line	λ (Å)	Observed flux (erg s^{-1} cm^{-2})	Error (erg s^{-1} cm^{-2})	rms (erg s^{-1} cm^{-2})	EW (Å)	FWHM (Å)	Luminosity (erg s^{-1})
He I	3188	1.74×10^{-16}	4.16×10^{-17}	1.01×10^{-17}	1.82	3.17	4.84×10^{39}
H16 + He I	3704	7.89×10^{-17}	1.10×10^{-17}	3.64×10^{-18}	1.04	3.68	2.19×10^{39}
[O II]	**3727**	$\mathbf{9.50 \times 10^{-15}}$	$\mathbf{4.74 \times 10^{-17}}$	$\mathbf{3.64 \times 10^{-18}}$	**132.49**	**4.08**	$\mathbf{2.64 \times 10^{41}}$
H12	3750	1.55×10^{-16}	9.31×10^{-18}	2.63×10^{-18}	2.17	3.72	4.31×10^{39}
H11	3770	2.09×10^{-16}	1.34×10^{-17}	3.99×10^{-18}	2.84	3.74	5.80×10^{39}
H10	3798	2.49×10^{-16}	1.86×10^{-17}	5.16×10^{-18}	3.40	3.77	6.91×10^{39}
H9	3835	3.38×10^{-16}	1.96×10^{-17}	4.83×10^{-18}	4.85	3.81	9.40×10^{39}
[Ne III]	**3868**	$\mathbf{2.96 \times 10^{-15}}$	$\mathbf{4.27 \times 10^{-17}}$	$\mathbf{5.56 \times 10^{-18}}$	**41.92**	**4.02**	$\mathbf{8.22 \times 10^{40}}$
He I + H8	3889	1.05×10^{-15}	2.96×10^{-17}	5.61×10^{-18}	14.75	3.88	2.91×10^{40}
[Ne III] + H7	3968	1.76×10^{-15}	2.40×10^{-17}	3.78×10^{-18}	23.46	5.47	4.87×10^{40}
[N II] + He I	4026	8.69×10^{-17}	1.25×10^{-17}	4.57×10^{-18}	1.14	4.00	2.41×10^{39}
[S II]	4069	1.30×10^{-16}	1.30×10^{-17}	4.10×10^{-18}	1.79	4.04	3.62×10^{39}
Hδ	**4102**	$\mathbf{1.54 \times 10^{-15}}$	$\mathbf{2.46 \times 10^{-17}}$	$\mathbf{4.07 \times 10^{-18}}$	**22.77**	**3.91**	$\mathbf{4.28 \times 10^{40}}$
Hγ	**4340**	$\mathbf{2.74 \times 10^{-15}}$	$\mathbf{2.60 \times 10^{-17}}$	$\mathbf{3.30 \times 10^{-18}}$	**43.08**	**3.93**	$\mathbf{7.61 \times 10^{40}}$
[O III]	**4363**	$\mathbf{5.32 \times 10^{-16}}$	$\mathbf{1.23 \times 10^{-17}}$	$\mathbf{2.79 \times 10^{-18}}$	**8.23**	**4.33**	$\mathbf{1.48 \times 10^{40}}$
He I	4471	2.16×10^{-16}	1.76×10^{-17}	4.71×10^{-18}	3.41	4.44	5.99×10^{39}
[Fe III]	4658	1.12×10^{-16}	1.99×10^{-17}	5.51×10^{-18}	1.76	5.86*	3.10×10^{39}
He II	4686	3.85×10^{-17}	9.35×10^{-18}	3.61×10^{-18}	0.62	4.65	1.07×10^{39}
[Fe III]	4702	3.61×10^{-17}	7.75×10^{-18}	2.79×10^{-18}	0.60	4.67	1.00×10^{39}
[Ar IV] + He I	4713	8.93×10^{-17}	1.16×10^{-17}	3.53×10^{-18}	1.50	4.68	2.48×10^{39}
Hβ	**4861**	$\mathbf{6.19 \times 10^{-15}}$	$\mathbf{3.54 \times 10^{-17}}$	$\mathbf{2.84 \times 10^{-18}}$	**117.91**	**4.97**	$\mathbf{1.72 \times 10^{41}}$
He I	4921	6.85×10^{-17}	1.18×10^{-17}	4.03×10^{-18}	1.34	4.89	1.90×10^{39}
[O III]	**4959**	$\mathbf{1.26 \times 10^{-14}}$	$\mathbf{5.82 \times 10^{-17}}$	$\mathbf{3.46 \times 10^{-18}}$	**228.19**	**4.86**	$\mathbf{3.49 \times 10^{41}}$
[Fe III]	4986	7.44×10^{-17}	1.40×10^{-17}	4.13×10^{-18}	1.36	4.95	2.07×10^{39}
[O III]	**5007**	$\mathbf{3.66 \times 10^{-14}}$	$\mathbf{1.12 \times 10^{-16}}$	$\mathbf{4.13 \times 10^{-18}}$	**623.15**	**4.88**	$\mathbf{1.02 \times 10^{42}}$
[N I]	5199	5.42×10^{-17}	7.16×10^{-18}	2.53×10^{-18}	0.98	5.16	1.51×10^{39}
He I	5876	7.54×10^{-16}	1.48×10^{-17}	2.29×10^{-18}	21.73	6.36	2.09×10^{40}
[O I]	6300	3.20×10^{-16}	7.35×10^{-18}	1.50×10^{-18}	7.88	6.26	8.88×10^{39}
[S III]	6312	9.25×10^{-17}	6.10×10^{-18}	1.50×10^{-18}	2.26	6.27	2.57×10^{39}
[O I]	6364	9.04×10^{-17}	3.21×10^{-18}	1.10×10^{-18}	2.21	6.32	2.51×10^{39}
[N II]	**6548**	$\mathbf{2.34 \times 10^{-16}}$	$\mathbf{7.85 \times 10^{-18}}$	$\mathbf{1.91 \times 10^{-18}}$	**6.96**	**6.50**	$\mathbf{6.49 \times 10^{39}}$
Hα	**6563**	$\mathbf{1.92 \times 10^{-14}}$	$\mathbf{5.03 \times 10^{-17}}$	$\mathbf{1.91 \times 10^{-18}}$	**583.63**	**6.30**	$\mathbf{5.34 \times 10^{41}}$
[N II]	**6583**	$\mathbf{6.99 \times 10^{-16}}$	$\mathbf{1.27 \times 10^{-17}}$	$\mathbf{1.91 \times 10^{-18}}$	**21.85**	**6.54***	$\mathbf{1.94 \times 10^{40}}$
He I	6678	2.54×10^{-16}	1.39×10^{-17}	2.72×10^{-18}	8.84	6.63	7.05×10^{39}
[S II]	**6717**	$\mathbf{1.16 \times 10^{-15}}$	$\mathbf{1.56 \times 10^{-17}}$	$\mathbf{1.92 \times 10^{-18}}$	**42.83**	**6.76**	$\mathbf{3.22 \times 10^{40}}$
[S II]	**6731**	$\mathbf{8.82 \times 10^{-16}}$	$\mathbf{1.42 \times 10^{-17}}$	$\mathbf{1.92 \times 10^{-18}}$	**33.14**	**6.86**	$\mathbf{2.45 \times 10^{40}}$
He I	7065	2.87×10^{-16}	1.38×10^{-17}	2.68×10^{-18}	9.83	7.01	7.97×10^{39}
[Ar III]	7136	5.43×10^{-16}	1.93×10^{-17}	3.03×10^{-18}	18.59	6.37	1.51×10^{40}
[O II]	**7320**	$\mathbf{2.78 \times 10^{-16}}$	$\mathbf{7.29 \times 10^{-18}}$	$\mathbf{1.57 \times 10^{-18}}$	**7.51**	**7.27**	$\mathbf{7.73 \times 10^{39}}$
[O II]	**7330**	$\mathbf{1.97 \times 10^{-16}}$	$\mathbf{6.87 \times 10^{-18}}$	$\mathbf{1.57 \times 10^{-18}}$	**5.38**	**7.28**	$\mathbf{5.47 \times 10^{39}}$
[S III]	**9069**	$\mathbf{7.00 \times 10^{-16}}$	$\mathbf{2.33 \times 10^{-17}}$	$\mathbf{7.41 \times 10^{-18}}$	**5.38**	**17.55**	$\mathbf{1.94 \times 10^{40}}$
[S III]	**9532**	$\mathbf{2.00 \times 10^{-15}}$	$\mathbf{2.21 \times 10^{-17}}$	$\mathbf{5.33 \times 10^{-18}}$	**17.28**	**18.44**	$\mathbf{5.55 \times 10^{40}}$

and then subtracted SN images with host templates through HOTPANTS. Photometric flux measurements were performed using the IRAF/DAOPHOT task and aperture photometry. We varied the aperture size until all of the SN flux was covered, then applied the same size for measuring the SN and standards. The zero-point was derived from five standard stars within the SDSS DR9 catalogue. Table 3 lists the photometry results. Due to poor weather conditions the LT images at +286 d yielded limiting magnitudes only.

The ACAM instrument on the WHT (camera specifications described in Section 2.1) provided deeper images at later times to allow us to recover the faint SN flux signal within the bright host galaxy. This was challenging as the SN flux was around 1 per cent of the host galaxy flux and the position of the PTF12dam is close to the brightest pixels in compact host. The analysis process as described for the RATCam data was used for the ACAM images. In this case there were 10 SDSS DR9 reference stars around the SN to calibrate the ACAM images. We again employed HOTPANTS to carry out target frame minus template subtractions, but the subtraction process was complicated by non-circular PSFs on some of the later frames. The last epoch for which we attempt to measure SN flux in (+400 d taken on 2013 August 25) proved to be challenging. The *i*-band image taken on this date (which we will call the

Table 3. Late-time photometry of PTF12dam and its host galaxy. The phase is in the SN rest-frame and it is days after *r*-band maximum (MJD = 56088). The '>' denotes that a detection was not made and the magnitude provided is the 3σ detection limit. The 'template' images are assumed to be the host galaxy only with no SN flux contribution. Optical *gri* magnitudes are in the AB system and the NIR JHK_s magnitudes are in the 2MASS Vega system.

Date	MJD	Phase	g	r	i	J	H	K_s	Telescope+Instrument
2013 Feb 20	56343.25	230.58				19.18 ± 0.19	18.81 ± 0.14	17.90 ± 0.19	NOT + NOTCam
2013 Mar 11	56362.26	247.75	20.86 ± 0.09	20.36 ± 0.04	20.83 ± 0.11				LT + RATCam
2013 Mar 23	56374.06	258.41				19.73 ± 0.16	19.16 ± 0.13	19.03 ± 0.18	NOT + NOTCam
2013 Apr 23	56405.06	286.41	>20.9	>21.4	>19.8				LT + RATCam
2013 Apr 26	56408.11	289.17				19.44 ± 0.12	19.61 ± 0.21	>19.3	NOT + NOTCam
2013 May 12	56424.05	303.57	21.36 ± 0.09						LT + RATCam
2013 May 20	56432.93	311.59		21.73 ± 0.09					LT + RATCam
2013 Jun 09	56452.96	329.68	22.25 ± 0.07	22.32 ± 0.04	22.12 ± 0.05				WHT + ACAM
2013 Jun 24	56467.03	342.39				20.12 ± 0.16	>18.7		NOT + NOTCam
2013 Aug 25	56529.90	399.19	23.97 ± 0.39	>24.1	23.33 ± 0.16				WHT + ACAM
Host template									
2014 Jan 22	56679.11	533.97	19.50 ± 0.08	19.11 ± 0.04	18.81 ± 0.03				WHT + ACAM
2014 Feb 09	56697.48	550.57	19.33 ± 0.04	19.00 ± 0.03	18.85 ± 0.03				LT+ RATCam
2014 Feb 13	56701.17	553.90				18.37 ± 0.15	17.82 ± 0.13	17.16 ± 0.09	NOT + NOTCam
2003 Feb 11	52681.47	pre-explosion	19.36 ± 0.02	19.20 ± 0.02	18.83 ± 0.03				SDSS DR9

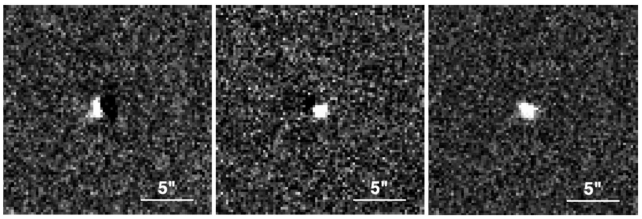

Figure 3. Image subtraction examples with the *i*-band images of latest epochs of PTF12dam. All images were taken from WHT + ACAM. Left: 20130825 − 20140122. Middle: 20130609 − 130825. Right: 20130609 − 20140122.

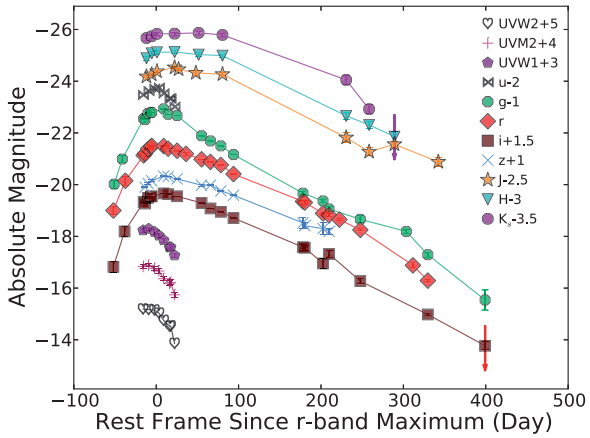

Figure 4. Absolute light curves of PTF12dam. Photometric points after +230 d were based on this work applying for the proper host subtraction and before +230 d were taken from Nicholl et al. (2013). Upper limits are shown with arrows of *r* and K_s bands at the last epochs. All points have been corrected for extinction, and *griz* magnitudes have also been *K*-corrected.

20130825 image for brevity) had a relatively large ellipticity, with an FWHM major/minor axes ratio of 1.04/0.86 arcsec. The *i*-band host galaxy template image, taken on 2014 January 22 (which we will call 20140122) has a more circular PSF, with axes ratios of 1.00/0.95 arcsec. We ran HOTPANTS with two different convolution directions, but in each of these cases it resulted in an attempted deconvolution along one of the minor or major axes directions. This produced poor quality difference images with visible dipole residuals (see left-hand panel of Fig. 3). Despite various attempts, no satisfactory result could be achieved to carry out the 20130825 − 20140122 image subtraction.

We thus employed an alternative approach. We subtracted the 20130825 and 20140122 images from the 20130609 image, which has a smaller and circular FWHM (major/minor axes measurements of 0.77/0.72 arcsec). This produced significantly better difference images (see middle and right-hand panel of Fig. 3), with no obvious residuals. The difference between the flux measured in the image 20130609 − 20140122 and that measured in 20130609 − 20130825 is then representative for our required epoch of 20130825 − 20140122. The *i*-band magnitude of the SN source in the difference image 20130609 − 20140121 is 22.12 ± 0.05, and in 20130609 − 20130825 difference image it is 22.56 ± 0.06, hence the magnitude of the SN in the 20130825 − 20140122 is $i = 23.33 \pm 0.16$ mag. The same analysis method and calculation was applied to the *g*-band data to give a final magnitude of 23.97 ± 0.39. There was no visible source detected in the *r*-band subtractions, and we set an upper limit of $r > 24.1$ mag.

The results are summarized in Table 3 and the absolute light curves, from UV to NIR, are plotted in Fig. 4. The early phases (before +230 d) were taken from Nicholl et al. (2013), and the late-time magnitudes are the results of the template subtractions carried out here. Due to the lack of late-time spectra of PTF12dam, we adopted the *K*-correction values from the final SN spectra around +200 d. There were $K_g = 0.24$, $K_r = 0.04$, and zero for *i* and JHK_s. The foreground ($A_V = 0.037$) and internal dust extinction ($A_V = 0.2$) are also corrected for. We discuss the estimate of host internal dust effect in the Section 3.1.

2.3.2 *Late-time spectroscopy of PTF12dam*

We took a spectrum of PTF12dam and its host galaxy with the 10.4-m GTC + Optical System for Imaging and low-Intermediate-Resolution Integrated Spectroscopy (OSIRIS) on 2013 December 25. The R500R grating was used (dispersion = 4.88 Å pixel^{-1}) with a central wavelength 7165 Å to cover the range from 4900 to 9200 Å. We used a 1.0 arcsec slit to obtain three spectra of 2400 s exposures

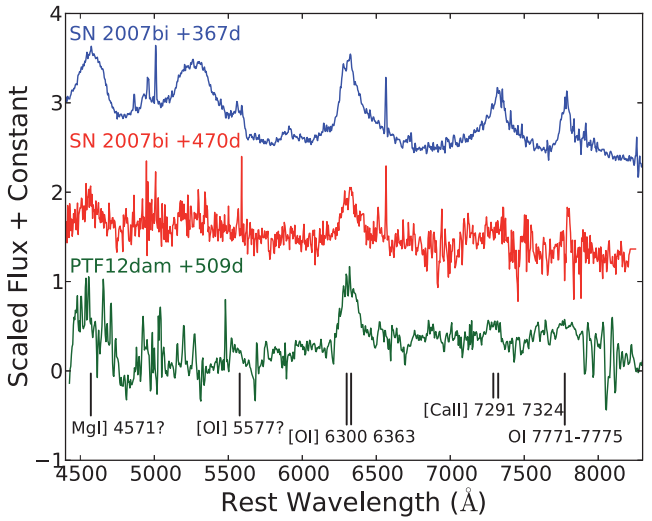

Figure 5. Spectrum of the host galaxy of PTF12dam at +508.6 d taken by GTC. Comparison with the late-time spectra of SN 2007bi from the WISeREP data base (Yaron & Gal-Yam 2012), which were published in Young et al. (2010), Gal-Yam (2012). Both wavelength and phases are stated in the SN rest frame.

each. All frames were reduced (overscan corrected, bias-subtracted and flat-fielded) though the IRAF package. The spectra were extracted using the standard IRAF routines, wavelength-calibrated by identifying lines of HgArXeNe arcs, and flux-calibrated by comparing with a spectroscopic standard star GD248. Telluric features were identified in reduced standard star spectra and subsequently removed from the SN spectra. The spectroscopic data are summarized in Table 1.

At this epoch, the SN was +508.6 d after the peak (rest frame) which means that the spectrum was dominated by emission lines and continuum from the host galaxy. Hence a method to retrieve any residual, broad lines in the SN nebular phase was required (e.g. see the nebular spectrum of SN 2007bi from Gal-Yam et al. 2009). We first scaled the flux of the GTC spectrum to match the host galaxy photometry with SDSS magnitudes. Then we applied a correction for the Milky Way reddening, shifted the spectrum to the rest frame, and applied an internal dust extinction correction (for all values used here, see Table 6).

We subtracted a galaxy continuum model, using the same method as in Nicholl et al. (2013). The population synthesis code STARBURST99 (Leitherer et al. 1999) was used to produce a model of a 30-Myr stellar population with continuous star formation, a metallicity of 0.05 $Z_{\odot}$ and a Salpeter IMF (further details in Nicholl et al. 2013). In order to be consistent with the previous and published result, we adopted the same metallicity model of the galaxy continuum, although the gaseous metallicity we measured is higher ($\sim$0.2 $Z_{\odot}$). We scaled the galaxy model to match the observed continuum in the observed spectrum, since we know the observed spectrum must be dominated by the host and the overall SN flux is around 1–2 per cent. This model was subtracted from the observed spectrum. Finally we removed the host galaxy emission lines by fitting them with Gaussian profiles and subtraction. This process left noise residuals at the positions of the strong lines, which we smoothed over with interpolation. Since we have a measurement of the SN flux in the i band from image subtraction, we scaled the resultant spectrum with a constant multiplicative factor so that it had a synthetic i-band magnitude of $i = 25.0$ (in the observer frame). The final spectrum, which is our best attempt at recovering the uncontaminated SN flux of PTF12dam (at an epoch of +509 d) is shown in Fig. 5. While this is understandably noisy, and the absolute flux of the SN continuum is uncertain, we do clearly detect the broad [O I] $\lambda\lambda$6300,6363 emission line feature from PTF12dam. The relative strength of this line is quite similar to that detected in SN 2007bi at +470 d. The host galaxy of SN 2007bi is some 3.4^{m} fainter than that of PTF12dam, hence the nebular spectrum of Gal-Yam et al. (2009) suffers much less host contamination. The identification of other features is more uncertain, but we label these possible detections in Fig. 5.

To quantitatively compare these emission lines to those of SN 2007bi, we fitted Gaussian profiles to the broad SN features to estimate flux, FWHM and EWs (again using our custom-built IDL suite of program PROCSPEC). The largest uncertainty in measuring the line flux comes from the positioning and definition of the continuum. We calculated values of the line flux and EWs from various reasonable continuum choices and different polynomial fitting functions (from order 1–3). The average values and the standard deviation of these are quoted in Table 4. The continuum positioning and choices were somewhat subjective and given the model subtraction and scaling, these flux and uncertainties should be treated with some caution. They are meant to illustrate that that we do detect the broad oxygen nebular lines in PTF12dam and give an approximate line flux.

The expansion velocities in Table 4 are the velocity values for the FWHM of the features. For the blended lines, we fitted single Gaussians and assumed that the two components were roughly equal in strength. The velocity estimated is a simple estimate of a deconvolved component of the doublet, assuming the intrinsic width of the component is just the separation between the lines. Since the GTC spectrum of PTF12dam is quite similar in morphology with the late-time spectra of SN 2007bi, we also measured the above properties for the [O I] $\lambda\lambda$ 6300,6363 line feature in SN 2007bi. All nebular line measurements are listed in Table 4. The line fluxes for SN 2007bi are significantly higher than those for PTF12dam, and the EW a factor of nearly 2 lower. This suggests that there is some host galaxy contamination in the last SN 2007bi spectrum of Gal-Yam et al. (2009). With the new measurements we now have of

Table 4. Flux measurements of the broad SN lines of PTF12dam in the GTC spectrum taken at +509 d. The [O I] line flux of SN 2007bi are reported for comparison.

SN name	Line	λ (Å)	Flux $\pm$ Error (erg s^{-1} cm^{-2})	EW (Å)	FWHM (Å)	Velocity (km s^{-1})	Luminosity $\pm$ Error (erg s^{-1})
PTF12dam (+509 d)	[O I]	5577	$7.0 \pm 0.5 \times 10^{-18}$	187	74	$\sim$4000	$1.9 \pm 0.2 \times 10^{38}$
	[O I]	**6300 6363**	$\mathbf{4.6 \pm 0.3 \times 10^{-17}}$	**332**	**137**	**$\sim$5800**	$\mathbf{1.3 \pm 0.1 \times 10^{39}}$
	[Ca II]	7291 7324	$1.1 \pm 0.1 \times 10^{-17}$	71	102	$\sim$4000	$2.9 \pm 0.3 \times 10^{38}$
	O I	7771–7775	$1.2 \pm 0.1 \times 10^{-17}$	78	109	$\sim$4200	$3.3 \pm 0.4 \times 10^{38}$
SN 2007bi (+470 d)	**[O I]**	**6300 6363**	$\mathbf{2.4 \pm 0.3 \times 10^{-16}}$	**190**	**143**	**$\sim$6100**	$\mathbf{9.5 \pm 1.0 \times 10^{39}}$
SN 2007bi (+367 d)	**[O I]**	**6300 6363**	$\mathbf{6.0 \pm 0.4 \times 10^{-16}}$	**358**	**182**	**$\sim$8100**	$\mathbf{2.4 \pm 0.2 \times 10^{40}}$

the host of SN 2007bi (see Section 2.1), this could be quantitatively addressed in future work.

3 HOST GALAXY PROPERTIES

3.1 Galaxy size, extinction corrections and luminosity

The profile of the host galaxy is noticeably broader than the stellar PSF, hence we can estimate a physical diameter of the extended source, assuming the relation (galaxy observed FWHM)^2 = (PSF FWHM)^2 + (intrinsic galaxy FWHM)^2. We measured the FWHM of both the host galaxy (1.48 arcsec) and the average (1.09 arcsec) of 10 reference stars within a 5 arcmin radius around the host in the SDSS *r*-band images taken on 2003 February 11. This provides a physical diameter of 1.9 kpc at the angular size distance 392.6 Mpc for $z = 0.107$ (Wright 2006), assuming a cosmology of $H_0 = 72\,\mathrm{km\,s^{-1}\ Mpc^{-1}}$, $\Omega_\mathrm{M} = 0.3$, $\Omega_\lambda = 0.7$. We also applied the same process for the *r*-band image taken from the WHT on 2014 January 22. The FWHM of the PTF12dam host was found to be 1.52 arcsec, and the seeing was 1.22 arcsec. We calculated the physical diameter of host to be 1.7 kpc, which is consistent with the result (1.9 kpc) from the SDSS pre-explosion image. Therefore, we adopted 1.9 kpc for the physical diameter of PTF12dam host as it was under a better seeing condition.

The absolute magnitude of the host is $M_g = -19.33 \pm 0.10$, after correcting for foreground extinction, *K*-correction and internal dust extinction corrections. The methods for these corrections are described as follows. First, in the optical, we adopted the apparent Petrosian magnitudes from the SDSS DR9 catalogue (Ahn et al. 2012) of the host galaxy (pre-explosion); for the UV bands, we adopted magnitudes from the *GALEX* GR6 catalogue (pre-explosion); for the NIR, we used our measurement of the host taken after +554 d from the SN peak. All photometric values are reported in Section 2.1. And then we applied a Milky Way extinction correction (Schlafly & Finkbeiner 2011) for each bandpass based on the value of $A_\mathrm{V} = 0.03$.

Next we determined *K*-corrections of the host using two methods. The first was using the recipes of Chilingarian, Melchior & Zolotukhin (2010) and Chilingarian & Zolotukhin (2012) with the SDSS colours. The second was using our own *K*-correction code (Inserra et al., in preparation) with the input spectrum of the host. All the corrections were minimal (less than a few hundredths of a magnitude) apart from the *i* band, which we calculated from our own code to have a correction of −0.06 mag. We also applied a *K*-correction to the *GALEX* magnitudes of FUV = −0.05 mag (from Chilingarian et al. 2010; Chilingarian & Zolotukhin 2012).

Moreover, we applied an internal dust extinction correction. We assumed a host extinction curve with $R_\mathrm{V} = 4.05$ that may be more appropriate for star-forming galaxies (Calzetti et al. 2000). The median SFR of their star-forming galaxy sample is 7.2 $\mathrm{M_\odot\ yr^{-1}}$, which is comparable with the SFR of the host of PTF12dam (5.0 $\mathrm{M_\odot\ yr^{-1}}$). We then used the intrinsic line ratio of Hα/Hβ = 2.86, Hγ /Hβ = 0.47 and Hδ /Hβ = 0.26 assuming case B recombination for $T_\mathrm{e} = 10\,000$ K and $n_\mathrm{e} = 100\,\mathrm{cm^{-3}}$ (Osterbrock 1989; Osterbrock & Ferland 2006), which implied an internal dust extinction of approximately $A_\mathrm{V} = 0.20$. Finally the absolute magnitudes were then calculated after these three corrections, using the luminosity distance of 481.1 Mpc and are listed in Table 6.

For comparison we also estimate here the equivalent values for the host of SN 2007bi. The H$\alpha$to Hβ ratio as published in the spectra of Young et al. (2010) implied a negligible internal dust extinction. Hence we only applied dereddening for the foreground extinction from the Schlafly & Finkbeiner (2011) Galactic dust map ($A_g = 0.09$) and then a *K*-correction ($g = -0.01$) from Chilingarian et al. (2010) and Chilingarian & Zolotukhin (2012). This resulted in absolute magnitudes (for a luminosity distance of 578.5 Mpc) of $M_g = -16.05 \pm 0.10$, $M_r = -16.49 \pm 0.06$, $M_i = -16.45 \pm 0.08$ and $M_z = -16.81 \pm 0.14$. The host of PTF12dam is some 3 mag brighter than that of SN 2007bi. As shown above, this complicates the recovery of SN flux at late times.

In addition, we measured the physical size of the host of SN 2007bi using the same method as employed above for PTF12dam. In the WHT *r*-band image on 2012 May 25, the seeing was 0.79 arcsec from the average of seven stars within a 1 arcmin radius around the host, while the FWHM of the host was 1.25 arcsec. Based on the angular size distance of the host of 455.5 Mpc, the physical diameter (derived from the observed galaxy FWHM) of the host of SN 2007bi is estimated to be 2.1 kpc.

3.2 Galaxy stellar mass

We employed the MAGPHYS stellar population model program of da Cunha, Charlot & Elbaz (2008) to estimate the stellar mass from the observed photometric points across UV, optical and NIR bands. The program employs a library of stellar evolution and population synthesis models from Bruzual & Charlot (2003) and fits the luminosity of the host stellar population.

The PTF12dam host spectrum is dominated by strong nebular emission lines which are not included in the model galaxy spectra of MAGPHYS. In order to estimate the appropriate broad-band magnitudes to input into MAGPHYS, the contribution of these emission lines need to be accounted for. We employed the WHT spectrum taken on 2013 March 30 to do this. One could simply remove the narrow emission lines from this spectrum and calculate synthetic photometry of the resultant spectrum to estimate the contribution from the lines. However this spectrum also contains some flux of PTF12dam (at +266-d rest frame) as discussed in Section 2. Therefore we carried out several experiments to estimate the emission line contamination to subtract from the SDSS pre-discovery host galaxy magnitudes. In the first instance, we attempted to remove the SN contribution by scaling the PTF12dam spectrum at +221 d by appropriate values estimated from the observed light curves (see Table 3) and subtracting this from the observed WHT spectrum. Secondly, we removed the emission lines in the WHT +266 d spectrum by fitting low-order polynomials across the base of the line widths and replacing the lines with these fits. We carried out synthetic photometry before and after removing the lines in the *gri* bands. To a level of accuracy of 0.1 mag, we found corrections to the *gri* bands of 0.2, 0.2 and 0.7 mag, respectively. This large correction for the *i* band is due to the major contribution of redshifted Hα, whereas the strong [OIII] lines fall in the *g*/*r*-band filter crossover point.

We used these *gri* continuum magnitudes along with the SDSS observed *z*-band magnitude, the *GALEX* FUV and NUV magnitudes and our measured JHK_s magnitudes from the last epoch described in Section 2.1 as measurements of the galaxy continuum from the FUV to the NIR. For the bands other than *gri* we did not apply any emission line correction since the galaxy spectra are dominated by continuum in the FUV and NIR and emission line contributions are not as strong as in the observed *gri* wavelength region. We used all of these bands as input to MAGPHYS (da Cunha et al. 2008), which determines a spectral energy distribution (SED) of the best-fitting model. This is simply the model with the lowest χ^2, estimated after allowing the physical input parameters to vary. The SED of the

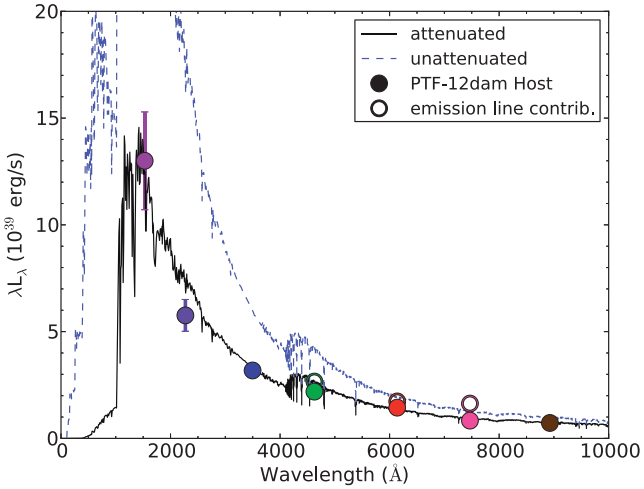

Figure 6. The best-fitting ($\chi^2 = 1.3$) SED of the host galaxy of PTF12dam from MAGPHYS (da Cunha et al. 2008), with (black line) and without (blue line) an attenuation by internal dust. The filled circles show the photometry from the galaxy continuum component, in the order of *GALEX* FUV, NUV and SDSS *ugriz* filter regions. Since there are no strong emission lines in FUV, NUV, *u* and *z* bands, we only removed the emission line contributions in *gri* bands. The open circles show their original photometric values of the host including emission line flux.

best-fitting model with $\chi^2 = 1.3$ is plotted in Fig. 6, which implies a stellar mass of 2.5×10^8 $M_\odot$. While the best fit, as defined by the χ^2 parameter, is useful for visualization of the model spectrum it does not represent the range of acceptable solutions or provide an uncertainty in the process. Therefore MAGPHYS also calculates the probability density function over a range of model values and determines the median and confidence interval corresponding to the 16th–84th percentile range. This is equivalent to the 1σ range, if the distribution is roughly Gaussian (see da Cunha et al. 2008, for details). As recommended by da Cunha et al. (2008), we take the best estimate of stellar mass to be this median 2.8×10^8 $M_\odot$ and the 1σ range to be from 2.3×10^8 to 3.7×10^8 $M_\odot$.

We examined the effect of our correction for emission line contamination and how the wavelength range of input photometry influences the results of MAGPHYS to determine the stellar mass of the galaxy. We used the *gri* photometry with and without the emission line contribution and we used different sets of wavelength restricted photometry as listed in Table 5. The results from using *ugriz* only and including the UV and NIR contributions are virtually identical which simply reflects the fact that the *ugriz* coverage is enough to constrain the SED, and the UV, optical and NIR flux are internally consistent with typical galaxy SEDs. The major difference arises in the inclusion of the nebular emission, which results in typically a factor of ∼2 difference in the median fits for mass. The χ^2 values for the best fits are also significantly better when using *gri* mag corrected for emission line flux. This illustrates the need to remove the emission line contribution and that this removal is more important than having wide wavelength coverage in the NUV and NIR. For comparison, we also fitted the galaxy SED model using the code Z-PEG (Le Borgne & Rocca-Volmerange 2002). We again used the UV and optical photometry of the galaxy with the emission lines removed and found the stellar mass of 3.3×10^8 $M_\odot$ for the best fit. The stellar mass estimation from Z-PEG is consistent to within 10 per cent with that from the MAGPHYS.

Table 5. Stellar mass determination from MAGPHYS. We listed the different input photometry settings and the corresponding SED best-fitting results. The main effect is removing or keeping the strong emission line contributions, which are equivalent to $g = 0.16$ mag, $r = 0.17$ mag and $i = 0.71$ mag.

Input photometry	Emission line	Best-fit χ^2	Median mass ($M_\odot$)
FUV, NUV, *ugriz*, JHK_s	Excluded	1.300	2.8×10^8
	Included	3.428	4.4×10^8
FUV, NUV, *ugriz*	Excluded	1.258	2.9×10^8
	Included	3.640	7.0×10^8
ugriz	Excluded	1.204	3.0×10^8
	Included	4.727	8.0×10^8
gri	Excluded	1.207	3.7×10^8
	Included	0.691	1.7×10^9

In summary we take the best estimate of the galaxy stellar mass to be $2.8^{+0.9}_{-0.5} \times 10^8$ $M_\odot$ from the median and equivalent 1σ uncertainty range from the probability density function of MAGPHYS.

For comparison we carried out a similar MAGPHYS analysis for the host galaxy of SN 2007bi with the observed *griz* photometry as discussed in Section 2.1. The stellar mass from the best-fitting model (which has a $\chi^2 = 0.031$) is 1.2×10^8 $M_\odot$ with $z = 0.127$. The 1σ likelihood distribution was from 1.1×10^8 to 2.0×10^8 around the median value of 1.4×10^8 $M_\odot$, which we adopt in the rest of this paper.

3.3 Age of the stellar population

MAGPHYS also calculates the *r*-band light-weighted age of the host stellar population. This is effectively an average age over all the stars in the galaxy. The light-weighted age is quantitatively defined in the equation from Gallazzi et al. (2005):

$$t_r = \int_0^t [\mathrm{d}\tau \psi(t-\tau) f_r(\tau) \tau] / \int_0^t [\mathrm{d}\tau \psi(t-\tau) f_r(\tau)], \quad (2)$$

where $f_r(\tau)$ is the total *r*-band flux radiated by stars of age τ, and $\psi(t)$ is the SFR. MAGPHYS gives an age of 44.7 Myr for the host of PTF12dam. For comparison, we also obtain stellar population age estimates using two other common methods.

First we used the Maraston (2005) simple stellar population models, which determine the age of the dominant stellar population in the host. We again used the synthetic photometry described above, after foreground extinction correction and removal of the host galaxy emission lines and SN continuum. We employed a metallicity of 0.5 $Z_\odot$ and assumed a Salpeter IMF with red horizontal branch morphology. The best-fitting result for the stellar population age is between 10 and 30 Myr.

Secondly, we used the rest-frame EW of Hα ($EW_{rest} = 527$ Å) to compare with the STARBURST99 models (Leitherer et al. 1999), assuming an instantaneous burst of star formation with a Salpeter IMF at solar metallicity. Such methods have also been employed recently to analyse the spectra of the environments of local SNe (Kuncarayakti et al. 2013). This resulted in a stellar population age around 30–40 Myr for the host of PTF12dam.

Taking these three estimates together, there appears to be a dominant young stellar population in the host, which is likely a common trend for SLSN Ic hosts. For instance, the stellar age for the host of SN 2010gx was estimated to be 20–30 Myr (Chen et al. 2013), and 5 Myr for the host of PS1-10bzj (Lunnan et al. 2013). This is not unexpected as the working assumption is these SLSNe Ic arise from

massive stars. However a quantitative restriction on the progenitor age (or mass) is not possible. The large range in the age estimates of the underlying population, and the fact that multiple epochs of star formation could have occurred in the last few Myr, means that more restrictive information on the progenitor systems is unlikely to be forthcoming from these population age studies. All that can confidently be determined is that a large population of stars younger than 30–40 Myr is present in the host of PTF12dam.

3.4 Metallicity of the host galaxy

We carried out an abundance analysis of the host galaxy based on the determination of the electron temperature derived from the [O III] λ4363 auroral line. First, the observed emission line flux (Table 2) were corrected for the foreground galactic ($A_V = 0.03$) and internal dust ($A_V = 0.20$) extinctions.

The [O III] λ4363 auroral line in the WHT spectrum (Fig. 2) is a strong, high signal-to-noise detection allowing us to estimate the electron temperature directly. We employed the task *temden* within the IRAF/STSDAS package to calculate the electron temperature from the line ratio of λλ4959, 5007/λ4363, given the electron density $n_e = 106$ cm^{-3} from the line ratio of [S II] λλ6717/6731 = 1.31. We thus determined T_e([O III]) ∼13 500 K ≡ T_3. Assuming a two-zone representation of the ionized region, this electron temperature is taken as the temperature in the high-ionization zone (T_3), and the value for electron temperature in the low-ionization zone (T_2) is determined as follows (from Garnett 1992):

$$T_2 = 0.7T_3 + 3000. \quad (3)$$

We thus obtained a $T_2 \sim 12\,400$ K.

As we have the electron temperature, electron density and flux ratios of [O II] λ3727, [O III] λ5007 lines relative to Hβ, respectively, we determined the ionic abundance of O^+ and O^{++} using the *nebular.ionic* routine within the IRAF/STSDAS package. The total oxygen abundances were then derived from the following equation:

$$\frac{O}{H} = \frac{O^+}{H^+} + \frac{O^{++}}{H^+}. \quad (4)$$

This provides an oxygen abundance of $12 + \log(O/H) = 8.04 \pm 0.09$ for the host of PTF12dam. For a solar value of 8.69 ± 0.05 (Asplund et al. 2009), this would imply that the host galaxy is 0.67 dex below solar abundance or 0.2 $Z_\odot$.

Due to the detection of He II λ4686, we checked if the amount of oxygen in the form of O^{+++} would influence the total oxygen abundance. The ionization potential of O^{++} is similar to that of He^+ (54 eV; Osterbrock 1989; Osterbrock & Ferland 2006), hence we can simply estimate the amount of O^{+++} from the ratio of the He II and He I recombination lines. We find that this would only increase the total oxygen abundance by 0.01 dex compared to the value from equation (4), and hence is a negligible contribution.

We also checked this with an alternate method for estimating T_2. Instead of calculating T_2 indirectly from equation (3), we used the ratio of nebular lines [O II] λλ3726, 3729 to auroral lines [O II] λλ7320, 7330 to estimate the electron temperature $T_2 \sim 14\,100$ K directly, which was derived from the *temden* task.

This method gives a value for T_2 which is somewhat higher than that for T_3, and strictly is not a consistent physical solution. However it is not uncommon in large observed galaxy samples (e.g. fig. 4a in Izotov et al. 2006) to see significant scatter in the T_2 and T_3 correlations and to have this situation. The reasons are unclear since the measurement uncertainties in the flux of all the lines are not too large (∼10 per cent at most). Despite this concern, if we calculate the abundance of O^+ and O^{++} using $T_2 \sim 14\,100$ K and $T_3 \sim 13\,500$ K, we determine a value of $12 + \log(O/H) = 8.00$, which is within the uncertainty of the value obtained initially.

As the nebular and auroral [S III] lines in the NIR and optical λλ9069, 9532/λ6312 were detected, we checked the electron temperature estimate from these for consistency. This gave an approximate value of ∼16 400 K, which is significantly higher than that derived from [O III] lines. We believe the discrepancy is due to the lower signal-to-noise of the [S III] lines, the fact that there is significant SN continuum in the NIR spectrum (since this spectrum was taken on +27 d after the peak), and the flux calibration is not as reliable as for our optical spectrum.

In order to calculate the sulphur abundance, we adopted the electron temperature derived from the [O III] lines ($T_3 \sim 13\,500$ K) and applied equation (3) to obtain $T_2 \sim 12\,400$ K. We used the *ionic* task to determine the S^{++}/H^+ and S^+/H^+ from the flux ratio of [S III] λ6312 and [S II] λ6717 lines relative to Hβ. We assumed that the total sulphur abundance is the sum of these two dominant ionic species, to give $12 + \log(S/H) = 6.17 \pm 0.12$. Hence, we calculated the $\log(S/O) = -1.87 \pm 0.12$ (using the T_e based oxygen abundance). This is slightly lower than the typical ratios in metal-poor galaxies in Izotov et al. (2006), which are in the range $\log(S/O) = -1.7 \pm 0.2$.

There are not many SLSN Ic host galaxies with metallicities determined by the direct method with electron temperature measurements. Hence in order to make comparisons, we also determined the metallicities from several commonly used diagnostics. The application of the R_{23} (M91) strong line method with the Kobulnicky, Kennicutt & Pizagno (1999) calibration, provides two possible estimates depending on whether the galaxy sits on the upper or lower branch of the calibration curve. These are 8.46 and 8.18, respectively. Since we have detected the auroral line, we can assume that we should be on the lower metallicity branch of the M91 relation. Hence the R_{23} oxygen abundance estimate is $12 + \log(O/H) = 8.18 \pm 0.03$. The other commonly used metallicity diagnostic is the N2 method (Pettini & Pagel 2004, hereafter PP04) which uses the N2 index = log([N II] λ6583/Hα). This method has the advantage that it is less affected by dust extinction, given the close wavelengths of the emission lines. The N2 index has a positive correlation with oxygen abundance and the metallicity derived from the PP04 calibration is consistent with that from the T_e method (Liang et al. 2007); we determined $12 + \log(O/H) = 8.10 \pm 0.02$ with the N2 method.

We further obtained a nitrogen-to-oxygen ratio $\log(N/O) = -1.32 \pm 0.13$ from the T_e calibration method, assuming that $N/O = N^+/O^+$. This places the galaxy close to the 'plateau' seen at $\log(N/O) \simeq -1.5$ on the N/O versus O/H diagram of galaxies (Pilyugin, Thuan & Vílchez 2003). For comparison, the mean values of oxygen and nitrogen abundances in 21 H II regions of the Small Magellanic Cloud are 8.07 ± 0.07 (T_e method) and log (N/O) of -1.55 ± 0.08 (from literature values summarized in Pilyugin et al. 2003). Hence the metallicity environment in the host galaxy of PTF12dam appears quite similar to that in the Small Magellanic Cloud.

Using the SN as an illuminating source provides a way to study the ISM inside the host galaxy. For example, Mg II λλ2796/2803 have been detected in some SLSNe Ic hosts (Quimby et al. 2011), and have been used to estimate the upper limit to the column density (Berger et al. 2012). Recently, Vreeswijk et al. (2014) detected resolved Mg II absorbers to study the host of iPTF13ajg. They found the strength of the Mg I and Mg II absorption in SLSN

hosts is lower than in GRB hosts. Here we detected absorption of the Mg II λλ2796/2803 doublet, which we presume is from the host galaxy. The two lines have the rest-frame EWs of 2.11 ± 0.27 and 2.01 ± 0.28 Å, respectively, in the WHT spectrum on 2012 May 25 at the SN phase: −13.6 d from the peak (Nicholl et al. 2013). The Mg II line centroids give almost identical redshifts ($z = 0.106$) to the [O III] emission lines ($z = 0.107$) detected in the same spectrum. The ratio of their measured line strengths is $W_{2796}/W_{2803} = 1.05$. The ratio of the oscillator strengths of these two transitions is close to 2, hence they are likely to be on the saturated part of the curve of growth which limits their use in diagnosing column densities in the host.

3.5 Star formation rate

After Milky Way and internal extinction correction, the observed flux of Hα is $F_{\rm H\alpha} = 2.29 \times 10^{-14}$ erg s^{-1} cm^{-2}. Applying the luminosity distance of $d_{\rm L} = 481.1$ Mpc (Wright 2006) of the host redshift ($z = 0.107$), we determined the luminosity $L_{\rm H\alpha} = 6.35 \times 10^{41}$ erg s^{-1}. We employed the calibration of Kennicutt (1998),

$$\mathrm{SFR(M_\odot\ yr^{-1})} = 7.9 \times 10^{-42}\, L(\mathrm{H\alpha})(\mathrm{erg\,s^{-1}}), \quad (5)$$

to determine the SFR of the galaxy to be 5.0 M$_\odot$ yr^{-1}. We also estimated the SFR from the [O II] λ3727 line flux for comparison, again using a calibration from Kennicutt (1998):

$$\mathrm{SFR(M_\odot\ yr^{-1})} = (1.4 \pm 0.4) \times 10^{-41}\, L([\mathrm{O\,II}])(\mathrm{erg\,s^{-1}}). \quad (6)$$

After correction for Milky Way and internal extinction and luminosity distance, the luminosity of the [O II] line is $L_{\rm [O\,II]} = 3.68 \times 10^{41}$ erg s^{-1} which gives 5.2 ± 1.5 M$_\odot$ yr^{-1}. This is consistent with the Hα measurement which further supports the use of [O II] λ3727 as an SFR diagnostic in higher redshift galaxies when Hα may be inaccessible if it is shifted into the NIR regime (Berger et al. 2012).

The *GALEX* FUV flux provides another way to estimate the SFR and to check for consistency between the methods (e.g. see Botticella et al. 2012, for a discussion of the comparison between the methods in the local volume). Corrections were applied for Milky Way extinction ($A_{\rm FUV} = 0.09$, $A_{\rm NUV} = 0.10$), *K*-correction (−0.05 mag for FUV, 0 mag for NUV) and internal extinction ($A_{\rm FUV} = 0.39$, $A_{\rm NUV} = 0.46$, assuming $R_{\rm V} = 4.05$) using the algorithm determined by Cardelli, Clayton & Mathis (1989) since Schlafly & Finkbeiner (2011) do not provide UV wavelength calibrations. We calculated a luminosity of $L_{1380\,\text{Å}} = 1.32 \pm 0.26 \times 10^{28}$ (erg s^{-1} Hz^{-1}), and then used the conversion of Kennicutt (1998) to estimate the SFR:

$$\mathrm{SFR(M_\odot\ yr^{-1})} = 1.4 \times 10^{-28}\, \mathrm{L_{FUV}(erg\,s^{-1}\,Hz^{-1})}, \quad (7)$$

which gives SFR =1.8 ± 0.4 (M$_\odot$ yr^{-1}). This is somewhat lower than that derived from Hα (5.0 M$_\odot$ yr^{-1}), and the discrepancy is in the opposite sense to that found by the Botticella et al. (2012) study which concluded that SFRs based on $L_{\rm FUV}$ appeared to be systematically higher (by nearly a factor 2) than those from $L_{\rm H\alpha}$.

Since the FUV luminosity is quite significantly affected by the internal dust extinction law (and value) applied, we considered that the Hα luminosity is less affected by dust extinction and there are more dwarf galaxy measurements to compare this method with, we will adopt the SFR = 5.0 M$_\odot$ yr^{-1} from Hα method as the value for the PTF12dam host galaxy throughout the rest of this thesis. Finally, the sSFR is defined as the SFR divided by stellar mass. We calculated the sSFR of the PTF12dam host to be 17.9 Gyr^{-1}.

Table 6. Main properties of the host galaxy of PTF12dam. All magnitudes listed are in the AB system, while the NIR magnitudes are converted from the Vega system (Blanton & Roweis 2007). Internal extinction with the rest-frame wavelength of *g* band.

SDSS name	SDSS J142446.21+461348.6
RA (J2000)	14:24:46.20
Dec. (J2000)	+46:13:48.3
Redshift	0.107
GR6 *GALEX fuv* (mag)	20.13 ± 0.19
GR6 *GALEX nuv* (mag)	20.13 ± 0.14
DR9 Petro *u* (mag)	19.79 ± 0.05
DR9 Petro *g* (mag)	19.36 ± 0.02
DR9 Petro *r* (mag)	19.20 ± 0.02
DR9 Petro *i* (mag)	18.83 ± 0.03
DR9 Petro *z* (mag)	19.32 ± 0.14
J (mag)	18.37 ± 0.15
H (mag)	17.82 ± 0.13
$K_{\rm s}$ (mag)	17.16 ± 0.09
K-correction$_g$ (mag)	∼0
Internal extinction$_g$ (mag)	∼0.20 ($R_{\rm V} = 4.05$)
Luminosity distance (Mpc)	481.1
$M_{\rm fuv}$ (mag)	−18.86 ± 0.20
$M_{\rm nuv}$ (mag)	−18.85 ± 0.14
M_u (mag)	−18.97 ± 0.07
M_g (mag)	−19.33 ± 0.10
M_r (mag)	−19.42 ± 0.04
M_i (mag)	−19.68 ± 0.06
M_z (mag)	−19.21 ± 0.14
M_J (mag)	−19.26 ± 0.15
M_H (mag)	−19.27 ± 0.13
$M_{K_{\rm s}}$ (mag)	−19.64 ± 0.09
Physical diameter (kpc)	∼1.9
12 + log (O/H) ($T_{\rm e}$) (dex)	8.05 ± 0.09
12 + log (O/H) (R_{23}) (dex)	8.18 ± 0.03
12 + log (O/H) (N2) (dex)	8.10 ± 0.02
N/O ($T_{\rm e}$)	−1.32 ± 0.13
S/O ($T_{\rm e}$)	−1.87 ± 0.12
Hα luminosity (erg s^{-1})	6.35×10^{41}
SFR (M$_\odot$ yr^{-1})	5.0
Stellar mass (M$_\odot$)	2.8×10^8
sSFR (Gyr^{-1})	17.9

By comparison, the SFR in the host of SN 2007bi is only 0.01 M$_\odot$ yr^{-1} from the Hα flux reported in Young et al. (2010); the PS1-11ap host has SFR = 0.47 ± 0.12 M$_\odot$ yr^{-1} estimated from the [O II] λ3727 line flux. All main physical properties of the host galaxy of PTF12dam are listed in Table 6.

3.6 Pixel by pixel analysis

Since the SLSNe Ic in Lunnan et al. (2014) show a wide diversity in the positions within the *Hubble Space Telescope* (*HST*) images of some of the host galaxies, we undertook a detailed pixel by pixel analysis of the host of PTF12dam to determine if it was located in the highest star-forming and densest stellar mass regions.

We used the optical *ugriz*-band images taken from the WHT + ACAM on 2014 January 22, +534 d (rest frame) after the peak. We assumed that the SN flux is negligible in the images. To extend the wavelength coverage for the SED fitting, we also took *u*- and *z*-band images (specifically the WHT ACAM filters: 700 SlnU, 704 SlnZ). We adopted 13 reference stars from the

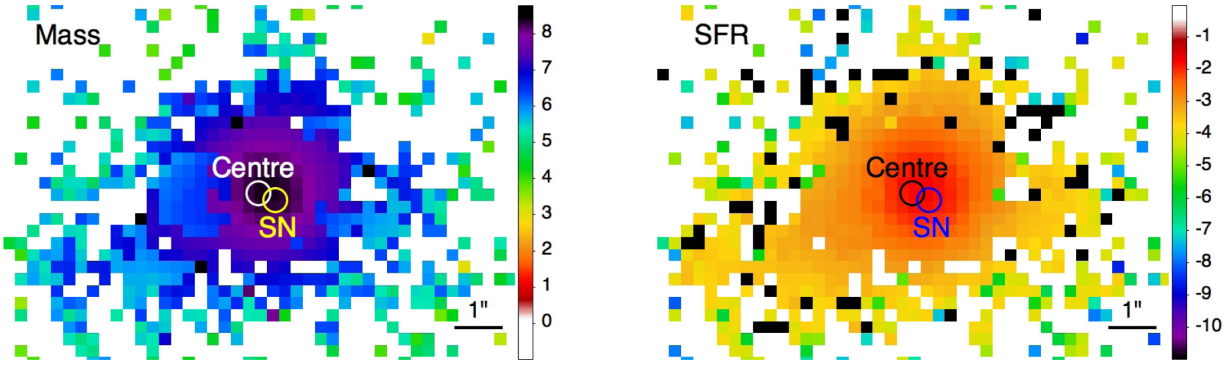

Figure 7. Five-band (*ugriz*) pixel–pixel study of PTF12dam host galaxy. Left: the variation in stellar mass distribution of the host. The colour bars indicate stellar mass from 10^0 to 10^8 $M_\odot$. Right: the variation in SFR distribution of the host. The colours show levels of SFR from 10^{-1} to 10^{-10} $M_\odot$ yr^{-1}. The host centre is defined by the brightest region of the combined optical band image and marked with a 0.25-arcsec size circle, the SN position is ∼0.4 ± 0.5 arcsec around the centre. The centre and SN positions are located in the densest areas of the stellar mass and SFR maps.

SDSS DR9 catalogue (Ahn et al. 2012) to set the photometric zero-points. Instead of measuring the whole galaxy flux, we chose an area (50 × 50 pixels) around the host galaxy centre and calculated their flux values pixel by pixel for each *ugriz*-band images. The stellar mass and SFR of each pixel were determined using MAGPHYS and we treated each individual pixel as a 'galaxy' in the MAGPHYS SED fitting: five-band (*ugriz*) flux of each pixel were compiled and fed into the MAGPHYS software. The input flux were Milky Way extinction corrected according to Schlegel, Finkbeiner & Davis (1998). There were no internal extinction priors assumed in the SED fitting. Note that since the emission line distribution in the host is not resolved, the flux are not emission line free.

Marginalized likelihood distribution of each physical parameter, e.g. stellar mass and SFR, of that pixel are then determined by comparison of the input SED with all the model galaxies' SEDs in the MAGPHYS library. Both SFR and stellar mass are determined using SED fitting based on the photometry of all five bands in MAGPHYS; see Section 3.2.

The maps are shown in Fig. 7 which give the median value (50 per cent) of the likelihood distribution, not the value of the best-fitting model. The SN position is very close to the optical centre of the host with a small 0.4 ± 0.5 arcsec offset. The most dense region in the stellar mass map is close to the optical centre of the host (as is the SN position) at a value corresponding to $10^{8.4}$ $M_\odot$. This also is the region of highest SFR (0.02 $M_\odot$ yr^{-1}). Recently, Lunnan et al. (2015) presented pixel statistics for 16 SLSN Ic hosts using *HST* UV images. They found that SLSNe Ic occur in overdense regions, in which a median SFR density is ∼0.1 $M_\odot$ yr^{-1} kpc^{-2}. However, in our case, the ground-based host images are seeing dominated, which means one should not interpret the real galaxy scale as being spatially resolved at finer detail in these images.

4 THE BOLOMETRIC LIGHT CURVE OF PTF12DAM FROM −52 TO +399 D

Nicholl et al. (2013) presented a bolometric light curve of PTF12dam from −52 to +222 d which included contributions from the UV (λ_c = 1928–2600 Å), optical (*ugriz*) and NIR (*JHK*$_s$). Here we extend this baseline out to 400 d (rest frame from the peak), to further test the competing models that have been developed to explain the extreme luminosity.

We used our measured late epoch *gri* and *JHK*$_s$ magnitudes (listed in Table 3) to calculate the bolometric luminosity of PTF12dam at +200 to +400d in the same way as Nicholl et al. (2013). The magnitudes were adjusted for Milky Way extinction (A_V = 0.04), *K*-corrections (calculated from the +221 d spectrum of Nicholl et al. 2013) and internal dust extinction of the host (A_V = 0.2). We chose to calculate the bolometric flux at every epoch with an *r*-band observed data point.[3] At these epochs, magnitudes in the available filters were converted to physical flux, and an SED was then constructed by linearly interpolating between the observed flux. If any of the *giJHK*$_s$ filter measurements were not available at the defined epoch, we estimated the magnitude by linear interpolation between the two closest points in time. This method provides a reliable measurement of bolometric flux from the *g* band through to K_s, but does not account for flux beyond these limits. Since the light-curve models of magnetar powering, pair-instability or CSM interaction provide calculations of total bolometric flux output (Kasen & Bildsten 2010; Kasen, Woosley & Heger 2011; Nicholl et al. 2013, 2014), we require a method to account for the UV and mid-infrared (MIR) contributions. The methods to determine the full bolometric light curve between 1600 Å and 4.5 μm are described below. Our analysis principle is to first use real, measured flux where possible. When data points are missing, we try to use measured data from similar SNe, and finally if that fails we use blackbody fits to cover portions of the SED where no observational data exist.

PTF12dam was observed by the Ultraviolet and Optical Telescope on the *Swift* and ground-based *u* band covering ∼1600–3800 Å but only until +22 d. To determine the UV contribution after this, we have a ready-made template in the SN PS1-11ap. This SN is at z = 0.524 and the observer frame g_{P1} and r_{P1} Pan-STARRS1 filters correspond approximately to the rest-frame filters $UVW1_{Swift}$ and u_{SDSS} (see McCrum et al. 2014). This provides measured $UVW1_{Swift}$ data to +83 d and u_{SDSS} data to +254 d. We assume that the relative UV flux of PTF12dam (compared to the optical) is similar to that of PS1-11ap which is justified given their similar spectra, light curve and colour evolution (Nicholl et al. 2013; McCrum et al. 2014). This provides measured flux for PS1-11ap down to 2250 Å in the NUV until +83 d and down to 3000 Å until +254 d. To calculate the flux contribution down to 1600 Å we fitted blackbody spectra to the observed SEDs defined by these filters (*UVW1,ugri*). This provided the flux contribution in the UV range (1600–3100 Å) compared to the optical of PS1-11ap during −36

[3] For the final epoch +399 d, we had only an upper limit in the *r* band, and hence we used the *i*-band magnitude as the primary reference magnitude instead.

to +254 d. In summary, we used the measured *Swift* UV data for PTF12dam when available (until +22 d) and used the UV flux contribution estimated for PS1-11ap from +25 to +254 d. Using the values between +100 and +254 d, we linearly extrapolated the UV contribution to provide estimates between +245 and +399 d. Hence we have a reasonable estimate of the UV flux of PTF12dam across the whole light curve of −52 to +399 d. The relative contribution is plotted in Fig. 9, showing the region of linear extrapolation. We know that the UV contribution to PTF12dam is not insignificant at these late times since the observed spectrum slope of PTF12dam at +221 d is still rising and has not turned over at 3000 Å (fig. 2 in Nicholl et al. 2013).

Further corrections are required to properly account for flux in the NIR and MIR. PTF12dam was observed in the NIR JHK_s bands to +258 d, allowing a full integration of the observed flux out to 2.3 μm over this period. A *J*-band measurement was available until +342 d, and an *H*-band measurement until +289 d. We used these points, but otherwise the JHK_s bands were linearly extrapolated to the dates necessary to allow a contribution to be calculated. Observations of the MIR flux of SNe have been limited to the very nearby explosions. We assume that the MIR contribution (i.e. beyond the red-edge of the K_s filter) for PTF12dam is negligible up to 150 d, but that it becomes significant afterwards which is supported by observations of nearby SNe (e.g. SN 2011dh, Ergon et al. 2014; SN 1987A, Bouchet et al. 1989). For all epochs after +150 d from the peak, we simply assumed that the MIR flux was 20 per cent of the total bolometric luminosity. This 20 per cent estimation is based on the MIR contribution to Type IIb SN 2011dh (Ergon et al. 2014) and is in reasonable agreement with the MIR contribution for SN 1987A in the early nebular phase (Hamuy et al. 1988; Bouchet et al. 1989). The lack of MIR data for other hydrogen poor Type Ibc SNe in the local Universe prevents any further comparison. We adopted the data from the Type IIb SN 2011dh, since it is a stripped envelope object with a very low mass hydrogen envelope. If we assume that the SN at late times was a blackbody emitter, the MIR flux contribution would be ∼20 per cent for a temperature of 3000 K, and ∼15 per cent for a temperature of 3500 K. Adoption of a 20 per cent contribution is admittedly somewhat arbitrary, but is probably the best estimate we have at this point. It is only likely to be significantly different if SLSNe Ic somehow show peculiar MIR emission compared to normal SNe.

The final bolometric light curve of PTF12dam is plotted in Fig. 8 and the data points are listed for reference in Table 7. The fraction of total luminosity in the UV, optical, NIR and MIR wavelength ranges using this method is illustrated in Fig. 9. Uncertainties are accounted for in the error bars in Table 7. These include the error in photometric measurements and an uncertainty arising from the extrapolation method for the missing filter data. The latter was estimated by comparing two different methods. The first was when we used linear extrapolation (or interpolation) of observed light-curve points to estimate a magnitude. The second was to assume a constant colour evolution from the nearest measured points in time (with respect to the *r* band) and apply this colour to get the missing filter data. The difference between the two is used as an error estimate.

There are differences between the bolometric luminosities calculated in this work and Nicholl et al. (2013) as illustrated in Fig. 8. We added the UV contributions based on PS1-11ap estimate after +25 d when there were no UV observations, whereas Nicholl et al. (2013) assumed a linear decline by extrapolating a fit to the last few observed points. Also we now have NIR JHK_s template images for the NOTCam images and can subtract the contribution of the host,

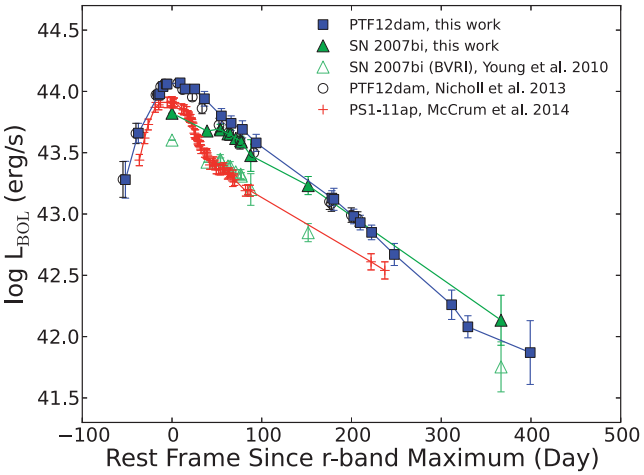

Figure 8. Bolometric light curves of PTF12dam, SN 2007bi and PS1-11ap. A true bolometric light curve of PTF12dam (integrating the estimated SED from the FUV to MIR) is shown as the filled blue squares. For reference, the previously published calculations of Nicholl et al. (2013) are plotted and the differences are discussed in Section 4. A similar, true bolometric light curve of SN 2007bi is shown using the *BVRI* broad-band photometry from Young et al. (2010) and a similar SED evolution as for PTF12dam. For comparison the pseudo-bolometric light curve presented in Young et al. (2010) is plotted, indicating what the likely correction is if flux in the UV and NIR/MIR is ignored. The bolometric light curve of PS1-11ap as calculated in McCrum et al. (2014) is plotted as red crosses. This is directly comparable with the true bolometric light curves of PTF12dam and SN 2007bi, although beyond +100–150 d it may be underestimated by 10–20 per cent due to lack of inclusion of an MIR contribution.

Table 7. Bolometric flux and uncertainty of PTF12dam and SN 2007bi. The SN phase is reported with respect to the observed maximum light in the rest frame.

PTF12dam		SN 2007bi	
Phase (d)	log L_{Bol} (erg s^{-1})	Phase (d)	log L_{Bol} (erg s^{-1})
−51.94	43.28 ± 0.15	0.00	43.82 ± 0.00
−37.49	43.66 ± 0.08	39.04	43.68 ± 0.00
−15.24	43.97 ± 0.03	53.77	43.69 ± 0.04
−13.62	43.98 ± 0.03	54.13	43.67 ± 0.02
−9.98	44.04 ± 0.03	62.38	43.65 ± 0.02
−6.38	44.06 ± 0.03	64.77	43.65 ± 0.04
−5.47	44.06 ± 0.03	70.98	43.62 ± 0.02
9.06	44.07 ± 0.03	76.57	43.60 ± 0.04
14.47	44.02 ± 0.03	77.20	43.59 ± 0.03
25.30	44.02 ± 0.03	87.76	43.48 ± 0.13
36.16	43.94 ± 0.06	151.73	43.23 ± 0.07
55.04	43.80 ± 0.06	366.64	42.13 ± 0.20
65.87	43.74 ± 0.06		
78.46	43.69 ± 0.07		
93.82	43.58 ± 0.07		
178.15	43.13 ± 0.06		
180.33	43.12 ± 0.09		
202.48	42.98 ± 0.06		
209.77	42.93 ± 0.06		
222.38	42.85 ± 0.06		
247.75	42.67 ± 0.09		
311.59	42.26 ± 0.12		
329.68	42.08 ± 0.09		
399.19	41.87 ± 0.26		

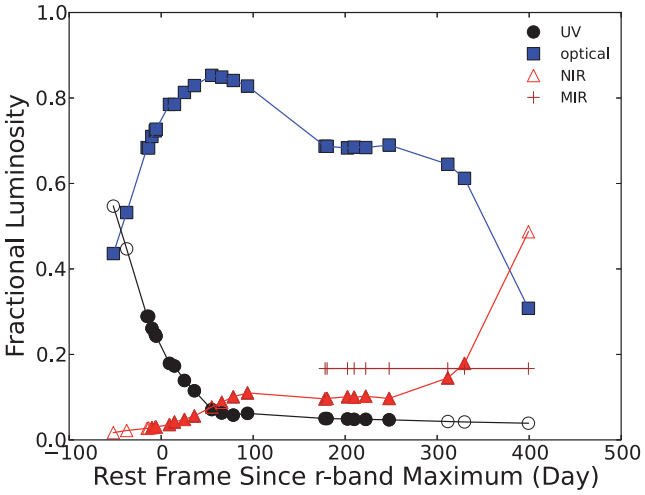

Figure 9. Relative contributions of the UV, optical, NIR and MIR flux of PTF12dam to its total luminosity. The filled symbols indicate where measured data points were used and the open symbols show the flux which were based on the extrapolation methods described. The MIR contribution of 20 per cent of the total flux was assumed.

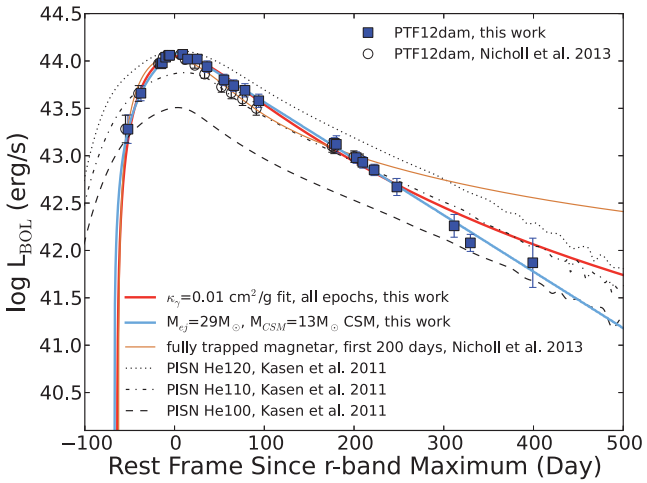

Figure 10. Bolometric light curve of PTF12dam and alternative models. The new bolometric light curve of PTF12dam is shown with blue squares and the new magnetar best-fitting model with $\kappa_\gamma = 0.01$ cm^2 g^{-1} is the red line. For comparison, the black circles show the bolometric light curve of PTF12dam from Nicholl et al. (2013), and their fully trapped magnetar model ($\kappa_\gamma = \infty$) is shown by the orange line. Background black lines illustrate PISN models (Kasen et al. 2011) of different mass, which are not fitted with the PTF12dam light-curve evolution. Our CSM model (blue line) is also present. See Section 5 for details.

which is significant at +200 d. The NIR data points in Nicholl et al. (2013) have some host contamination and hence they are higher by a factor of 1.3–1.5 compared to our values, after host subtraction. However, this is offset due to the fact that we estimate a higher UV contribution. Overall then, the combination of these two factors results in a similar bolometric light curve as shown in Nicholl et al. (2013) for the epochs up to +220 d.

To allow a like-for-like comparison, we estimated the bolometric light curve of SN 2007bi over the same wavelength range as PTF12dam, using as similar a method as possible. We adopted the *BVRI* photometry from Young et al. (2010), dereddened it by the Milky Way extinction of $A_V = 0.08$, performed *K*-corrections using values from Young et al. (2010), and assumed internal dust extinction is negligible (as suggested from Hα and Hβ line ratio). Due to the paucity of data around peak, we simply assumed a constant colour with *R* for the *B*, *V* and *I* light curves. We also assumed that SN 2007bi has a similar multicolour photometric evolution as PTF12dam, and therefore that the percentage contributions in the UV and NIR, as a function of time, are the same (as in Fig. 9). We assumed a 20 per cent MIR contribution to the data at epochs later than +150 d after peak. These are also plotted in Fig. 8, and as expected we find higher values than Young et al. (2010). This is simply due to our accounting for flux outside the *BVRI* bands.

5 DISCUSSION : THREE ALTERNATIVE LIGHT-CURVE MODELS

5.1 Magnetar model

The extension of the bolometric light curve to these quite late phases allows us to test the magnetar and ^{56}Ni powering mechanisms as both make different predictions for the very late phases. These new points show that the late-time luminosity of PTF12dam declines more rapidly than the spin-down luminosity of the magnetar model which was used to fit the early-time data in Nicholl et al. (2013). However this model assumes 100 per cent efficient trapping of the magnetar energy in the ejecta. For a magnetar with parameters from that fit ($M_{ej} = 16\,M_\odot$, $P_{ms} = 2.6$ ms, $B_{14} = 1.14 \times 10^{14}$ G, and using $\kappa = 0.1$ cm^2 g^{-1}) to be able to reproduce the observed behaviour at late epochs, escape of gamma-ray radiation must be postulated. This escape must begin at around +200 d post-explosion.

The trapping and thermalization of the high-energy radiation being emitted from the interface of the pulsar wind nebula and the SN ejecta is a poorly understood process, with only Kotera, Phinney & Olinto (2013) and Metzger et al. (2014) having discussed the physical situation for the case of fast-spinning and highly magnetized pulsars. Assuming that the opacity for the high-energy radiation is dominated by pair production (high-energy gamma rays) the relevant opacity is of order $\kappa_\gamma = 0.01$ cm^2 g^{-1} (Longair 1992).

Fig. 10 shows the best-fitting magnetar model assuming a trapping with this opacity and the trapping function of Arnett (1982). The model does a good fit of reproducing the full light curve. The loss of trapping begins around 100 d and is a factor ~10 at 400 d. In this case the parameters of the best-fitting model are different to those in Nicholl et al. (2013). We required $M_{ej} = 10.50\,M_\odot$, $P_{ms} = 2.72$ ms, $B_{14} = 0.69 \times 10^{14}$ G for our new magnetar model. The opacity of the ejecta and the physical nature of the energy coupling with the putative pulsar wind is an area worthy of further, more detailed study. Here we merely show that the light-curve decline rate at +200–400 d can plausibly be explained if high-energy gamma rays are created at the base of the SN ejecta, as the opacity for such radiation (pair production) leads to partial escape after a few months.

5.2 Pair-instability supernova model

In Nicholl et al. (2013) it was shown that the rise time of PTF12dam is significantly shorter than in PISN models. Fig. 10 shows that also the decline rate is faster than in PISN models (e.g. Kasen et al. 2011). Due to their high ejecta masses, gamma-ray trapping is complete in PISN models for several years, and their light curves therefore follow the decline rate of ^{56}Co (1 mag per 100 d). PTF12dam on the other hand declines by over 1.5 mag per 100 d between 100 and 400 d. Thus, both the rising and declining parts of the light

curve are inconsistent with a pair-instability ejecta, and can only be reproduced with models with significantly lower ejecta mass.

5.3 CSM model

An alternative model sees the light curve of PTF12dam powered by interaction of the SN ejecta with optically thick circumstellar gas. Nicholl et al. (2014) used the physical model of Chatzopoulos, Wheeler & Vinko (2012) combined with the Arnett (1982) diffusion treatment to calculate a series of models powered by interaction. In this scenario, the collision of the rapidly expanding ejecta with a massive, slow-moving CSM (approximated as stationary) launches forward and reverse shocks into the CSM and ejecta, respectively, which convert the kinetic energy of the expanding ejecta to thermal energy behind the shocks. The observed light curve is then produced by outward diffusion of this energy. Shock heating terminates when the two shocks have passed through all of the CSM and ejecta, after which time (in the absence of additional power sources, such as ^{56}Ni) the light curve decays exponentially. Nicholl et al. (2014) applied this model to the PTF12dam light curve up to 200 d after maximum, finding a good fit for $M_{\rm ej} = 26$ M$_\odot$ and $M_{\rm csm} = 13$ M$_\odot$. Here we used the same model calculations as in Nicholl et al. (2014) and fitted the light curve up to day 400, with our improved UV, NIR and MIR corrections, and recover very similar fit parameters ($M_{\rm ej} = 29$ M$_\odot$ and $M_{\rm csm} = 13$ M$_\odot$).

In order to distinguish the statistical significance of any difference between observations and models, we calculated the decline rate of the best fit of our new bolometric data points of PTF12dam from +50 to +400 d. Each data point was represented by Gaussian profile, centred on the measured luminosity and with a width of the error bars. We employed a Monte Carlo simulation to add random points in these Gaussians, and fitted straight lines to these simulated points. This process was repeated 10 000 times. Finally we measured the best-fitting gradient of 0.015 ± 0.001 mag d^{-1}. The error includes both the dispersion in the points and the individual errors. We compared the best-fitting result with the slope of PISN models, in the late-time phase, derived by ^{56}Co decay of 0.0098 mag d^{-1}. The decline rate of these three PISN models is about 0.011 mag d^{-1} around +100 to +400 d, which is not consistent with the gradient of PTF12dam. For the fully trapped magnetar model, the slopes are 0.011, 0.007 and 0.005 mag d^{-1} during +100 to +200 d, +200 to +300 d and +300 to +400 d, respectively. During the same duration, the slopes are 0.015, 0.012 and 0.010 mag d^{-1} of our new magnetar model with $\kappa_\gamma = 0.01$ cm^2 g^{-1}. This fits with the data relatively well, and passes through all observed points, except two points around +300 d. The slope of CSM model is 0.015 mag d^{-1}, and this does match the best-fitting gradient of PTF12dam. However, the CSM model required $M_{\rm ej} = 29$ M$_\odot$ and $M_{\rm csm} = 13$ M$_\odot$. Such a large amount of CSM material has only been quantitatively predicted by the pulsational PISN model (Woosley, Blinnikov & Heger 2007), which requires a progenitor mass between 95 and 130 M$_\odot$ (also see Heger & Woosley 2002; Heger et al. 2003).

Overall, fitting of the full light curve is consistent with our new magnetar model with low κ_γ. This goes through the majority of our new bolometric light-curve points and only two points were slightly discrepant. The ejecta mass estimated from the magnetar model is more than 10 M$_\odot$, hence the progenitor mass must be significantly larger. Heger et al. (2003) calculated that a massive single star more than 25 M$_\odot$ should collapse to a black hole. This might suggest that the progenitor mass should be more than 10 M$_\odot$ but less than 25 M$_\odot$ to be consistent with the ejecta mass measurement, and stellar evolution theory.

6 DISCUSSION : THE HOST GALAXY OF PTF12DAM

Amorín et al. (2014) presented a large sample of 183 EELGs, which have large [O III] λ5007 EWs and low metallicities (median of ∼0.3 Z$_\odot$). The host galaxy of PTF12dam would be defined as an EELG given the strengths of the classic nebular lines. For example the [O III] λ5007 line is unusually strong and with EW$_{\rm rest} \geq 563$ Å it has the highest EW of any host galaxy of SLSNe Ic within $z < 0.5$ (Lunnan et al. 2014; Leloudas et al. 2015). Leloudas et al. (2015) measured the EW$_{\rm rest} = 794$ Å for the [O III] λ5007 line using their pure galaxy spectrum taken on +567 d from the SN peak. At $M_g = -19.33$ the host of PTF12dam is also the brightest host galaxy of any SLSNe Ic detected within $z < 0.5$ (Lunnan et al. 2014; Leloudas et al. 2015).

Fig. 11 shows the luminosity–metallicity relationship for nearby dwarf galaxies with measured abundances with the $T_{\rm e}$ method. We choose to plot only results from this method, given the large offsets and calibration issues when the strong lined methods are used, e.g. the R_{23} or N2 method (Bresolin 2011). There are only four SLSN Ic hosts which have oxygen abundances measured by the direct method: PTF12dam, SN 2010gx (Chen et al. 2013), PS1-10bzj (Lunnan et al. 2013) and SN 2011ke (Lunnan et al. 2014). Since there is typically less than 0.1 mag difference between B and g magnitudes, we simply plot M_g on the same axis with no conversion for these four galaxies. On this plot, the four SLSN hosts lie at the extreme lower end of the oxygen abundance distribution for their equivalent M_B. In other words they appear not just to be low-metallicity dwarf galaxies, but to have peculiarly low oxygen abundances for dwarf galaxies. They occupy the same area as the four GRB host galaxies which have $T_{\rm e}$ determined oxygen abundances from Modjaz et al. (2008). This quantitatively supports the results from the extensive sample in Lunnan et al. (2014) that SLSN Ic host galaxies are similar to those of GRBs. Although we should bear in mind the caveat that the four GRB hosts in Fig. 11 were selected by Modjaz et al. (2008) to be nearby and have associated SNe detected. Lunnan et al. (2014) showed a similar plot of oxygen abundance versus host galaxy mass, which shows 15 SLSN Ic hosts measured with the R_{23} method. However due to the double value possibility in the R_{23} method, many of the points have large uncertainties in their absolute values. The work here shows that when the $T_{\rm e}$ direct method is applied, these quite extreme low metallicities hold up to scrutiny. The conclusion of Lunnan et al. (2014) that they are quantitatively similar to GRB galaxies (at least low redshift GRBs) is supported by the comparison in Fig. 11.

With an absolute magnitude of $M_g = -19.33 \pm 0.10$ the host of PTF12dam shows very similar properties to GP galaxies, which are star-forming, luminous compact dwarf galaxies (Cardamone et al. 2009). It lies close to the locus of points of GP galaxies in Fig. 11 and the physical parameters are similar. GPs typically have low mass (∼$10^{8.8}$ M$_\odot$), high sSFR (1–100 Gyr^{-1}) and low metallicity (∼0.2 solar abundance; see Izotov, Guseva & Thuan 2011). Amorín, Pérez-Montero & Vílchez (2010), estimated a mean value of $12 + \log({\rm O/H}) = 8.05 \pm 0.14$ for a sample of 79 star-forming GPs from the $T_{\rm e}$ method. The host of PTF12dam has the same metallicity as the mean value of GPs, a slightly lower stellar mass of $10^{8.4}$ M$_\odot$ and an sSFR of 17 Gyr^{-1} which is on the high end of the GP distribution. In the Baldwin, Phillips & Terlevich (1981) diagram, the host of PTF12dam is located in the starburst region with line ratios $\log$([O III] λ5007/Hβ) = 0.77 and $\log$ ([N II] λ6583/Hα) = −1.41. Again, this is similar to the GP distribution and close to the starburst/AGN boundary area. Also fig. 3 in Leloudas et al. (2015)

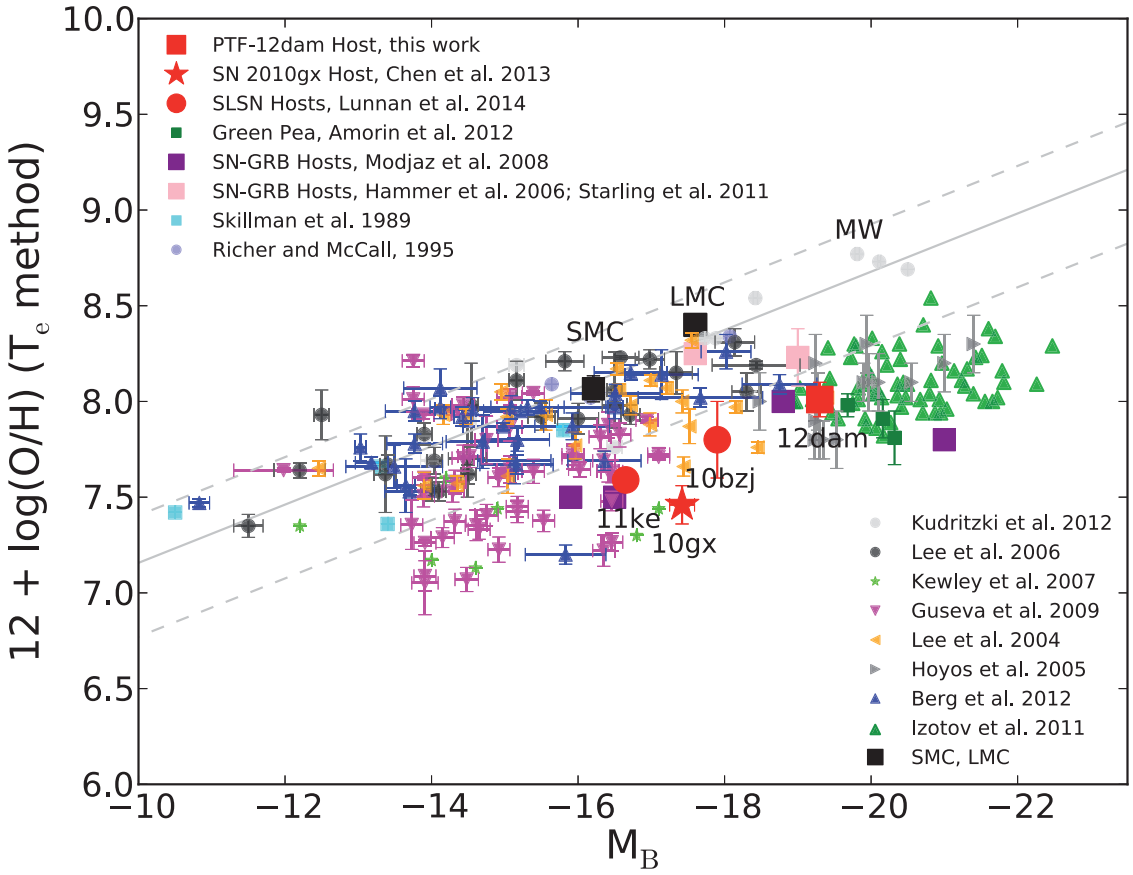

Figure 11. Luminosity–metallicity relationship for dwarf galaxies in the local Universe. Metallicity measurement was derived from the T_e direct method. Only four host galaxies of SLSNe Ic have direct oxygen abundance measurement so far; they all lie on the metal-poor edge compared with the local dwarf galaxies. We adopted metallicity values from the literature as follows: Skillman, Kennicutt & Hodge (1989), Richer & McCall (1995), Lee, Salzer & Melbourne (2004), Hoyos et al. (2005), Lee et al. (2006), Kewley et al. (2007), Guseva et al. (2009), Amorín et al. (2012), Berg et al. (2012). Grey lines are the boundary of normal galaxy mass–metallicity relation adapted from Kudritzki et al. (2012), with metallicities calculated using blue supergiants. GRB-SN events include GRB020903, GRB030329/SN2003dh, GRB031203/SN2003lw and GRB060218/SN2006aj from Modjaz et al. (2008); GRB980425/SN1998bw (Hammer et al. 2006), GRB100316D/SN2010bh (Starling et al. 2011).

presented a comprehensive sample including SLSN, GRB hosts and EELGs, which supports this comparison. The nitrogen/oxygen abundance ratio $\log(\mathrm{N/O}) = -1.38 \pm 0.13$ of the PTF12dam host is also similar to GPs (see fig. 2 in Amorín et al. 2010). The high-ionization lines He II λ4686 and [Ne III] λ3869, are detected in the PTF12dam host galaxy which is unusual but not unprecedented in SN and GRB host galaxy spectra (Savaglio, Glazebrook & Le Borgne 2009).

The host of PTF12dam is a low-mass galaxy of 2.8×10^8 $M_\odot$, consistent with the mean mass value of 31 SLSN Ic hosts from Lunnan et al. (2014) of 2×10^8 $M_\odot$. Lunnan et al. (2014) used the FAST stellar population synthesis code (Kriek et al. 2009) and fitted the SEDs with the stellar libraries of Maraston (2005). For PTF12dam they derived a value of $5.9^{+0.2}_{-0.5} \times 10^8 M_\odot$, which is a factor of 2 higher than what we estimate. In our detailed comparison of methods, we showed that although a wider wavelength coverage is useful, it is more critical to remove the contribution of emission lines to broad-band photometric measurements when applying models based on stellar population synthesis (for example the MAGPHYS code we employed here). Hence it is likely that the difference is due primarily to the inclusion of emission line flux in the broad-band photometry used by Lunnan et al. (2014), although our inclusion of UV and NIR data also improves the reliability of the mass inferred.

By comparison, the average stellar mass of GRB hosts of 46 objects from Savaglio et al. (2009) is 2.0×10^9 $M_\odot$, and Svensson et al. (2010) derived a median mass from their 34 GRB host sample of 1.3×10^9 $M_\odot$ derived from AB absolute K-band magnitude. Although it would initially appear that the host of PTF12dam is about 10 times less massive than these GRB host galaxies, the different methods employed can cause significantly different results. Savaglio et al. (2009) provided a calibration relation between stellar mass and M_K luminosity. Applying this, we would determine a mass for the PTF12dam host of 7.9–9.9 $\times 10^8$ $M_\odot$ (without and with K-correction for M_K), which is a factor of 2–3 more massive than that from the full SED fitting. Hence comparison between results from different methods should be done with some caution.

Thöne et al. (2014) also studied the host galaxy of PTF12dam. They used the OSIRIS spectroscopy at the 10.4 m GTC to observe the host after +567 d from the SN peak. They claimed that the SN position was resolved in their long-slit image and found a very young (∼3 Myr) stellar population at the SN site, which implied the progenitor of PTF12dam was a massive star (> 60 $M_\odot$) from this recent starburst. However, there was no detection of the

Wolf–Rayet (W–R) features in their host spectra at the SN site. The W–R feature has been known to be a good tracer of recent massive star formation (Kunth & Sargent 1981). There is a possible blue bump around 4640 Å in our late-time (+508 d) spectrum of PTF12dam (see Fig. 5), which was taken from the GTC with 2.6 times longer exposure time (2400 s × 3) than the Thöne et al. (2014) spectrum. These features are usually identified as N III and C III/C IV emission lines from W–R stars. Nevertheless, our GTC spectrum was very noisy at this edge region, and we cannot confirm this feature. In addition, there are also no W–R bumps in our main WHT spectrum (Fig. 2). Although some [Fe III] emission lines shown in the spectrum, they are very weak and narrow (e.g. EW of [Fe III] λ4658 ∼ 1.76 Å, [Fe III] λ4986 ∼ 1.36 Å). Brinchmann, Kunth & Durret (2008) analysed the galaxies with W–R features from the SDSS data base, and found that the main distribution of the widths of W–R lines are from 1000 to 3000 km s^{-1} FWHM from the He II λ4686 line. We measured the width of the He II line in our WHT spectrum to be ∼300 km s^{-1} FWHM. In summary there are no clear detections of the W–R features in our spectra, neither the broad W–R lines nor a broad component in the He II line.

We investigated three separate methods to determine the SFR in the host of PTF12dam and show that the SFR from Hα (5.0 M$_\odot$ yr^{-1}) is different to that from the FUV (1.8 M$_\odot$ yr^{-1}). This might not necessarily be physically consistent. The Hα/Hβ flux ratio could suggest that the photons arising in H II regions suffer from different extinction to continuum FUV photons as traced by the stellar continua of B-type stars. We also showed that using [O II] luminosity in this type of star-forming galaxy gives a result that is consistent (5.2 M$_\odot$ yr^{-1}) with that from Hα luminosity. This is useful when working at higher redshifts ($z > 0.5$) when Hα is shifted to the NIR and [O II] λ3727 is still accessible in the optical. The large SFR for PTF12dam is one of the highest measured for a SLSN Ic hosts (Lunnan et al. 2014), which is not unexpected given the strength of the emission lines. When combined with the mass measurement, the PTF12dam host galaxy has a very high sSFR (17.9 Gyr^{-1}), which is higher than that of field galaxies at the same redshift. Fig. 12 shows a comparison between GRB and CCSN hosts, SLSN Ic and the three 2007bi-like SN hosts that have been published to date. The host of PTF12dam has a high star-forming activity compared to the hosts of SN 2007bi and PS1-11ap. The stellar masses are quite similar although PS1-11ap is more massive. The sSFR of PTF12dam host is high, 50 times that of PS1-11ap's and up to 250 times higher than SN 2007bi's host.

The physical parameters of the hosts of these SN 2007bi-like SNe are also listed in Table 8. We recalculated the physical size (D) of the PS1-11ap host galaxy of ∼1.5 kpc using the angular size distance 1255 Mpc instead of the luminosity distance (2914 Mpc) used in McCrum et al. (2014). For SN 2007bi and PS1-11ap we had to use the R_{23} method since the [O III] λ4363 line was not detected. We adopted the low branch solution since log ([N II] /[O II]) < 1.2 (following Kewley & Dopita 2002). The hosts of PTF12dam, PS1-11ap and SN 2007bi span the full range of stellar mass and SFR that other SLSNe Ic occupy. They are all star-forming dwarf galaxies, with low metallicity and young stellar populations but they don't appear to be significantly different (nor self-similar) in comparison to the other SLSNe Ic. One should recall that SN 2007bi was initially suggested to be a pair-instability explosion by Gal-Yam et al. (2009) and PS1-11ap and PTF12dam are extremely similar in their properties. These three are the only well-studied SLSNe Ic which have slowly fading light curves and are the only possible PISNe candidates in the local Universe with published data. However we can

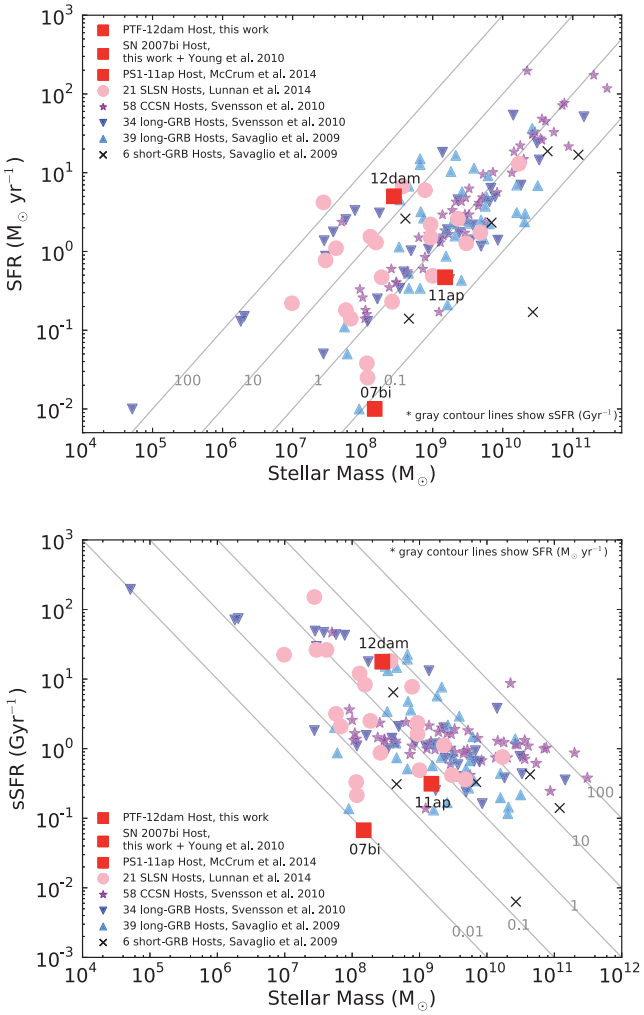

Figure 12. Stellar mass versus SFR (top) and sSFR (bottom) for SLSNe Ic (Lunnan et al. 2014), GRB (Savaglio et al. 2009; Svensson et al. 2010) and CCSN hosts (Svensson et al. 2010). The three red boxes show the locations of the three slowly fading SLSNe Ic published to date (Young et al. 2010; McCrum et al. 2014).

conclude that their host environments do not show any systematic difference from the bulk of SLSNe Ic.

The lowest metallicity host of any type of SN to date has been found to be that of SN 2010gx at $12 + \log(\mathrm{O/H}) = 7.4 \pm 0.1$ ($Z = 0.05\,Z_\odot$) on the T_e method scale (Chen et al. 2013). The host of PTF12dam also follows this low-metallicity trend. As discussed by Chen et al. (2013) and Lunnan et al. (2014), it appears that low metallicity is a fundamental requirement to producing SLSNe Ic. Only one out of the Lunnan et al. (2014) sample has a possible normal, solar like, metallicity (MLS121104) but this estimate is based on R_{23} and the SN is significantly offset from the possible host. The agglomeration of current evidence is now strongly suggestive that low metallicity, with a critical value of around 8.0 dex is required to produce SLSNe Ic, including the fast declining SN 2005ap/SN 2010gx types and the more slowly evolving SN 2007bi/PTF12dam-type explosions.

7 CONCLUSIONS

The host galaxies of SLSNe Ic seem to be exclusively compact, low mass, highly star-forming and of low metallicity. This poses a

Table 8. Host galaxy properties comparison of the three 2007bi-like SNe known to date.

SN	z	M_g (mag)	A_V (mag)	D (kpc)	SFR ($M_\odot$ yr^{-1})	M ($M_\odot$)	sSFR (Gyr^{-1})	$12 + \log$(O/H) (T_e) (dex)	$12 + \log$(O/H) (M91) (dex)	Reference
PTF12dam	0.107	-19.33 ± 0.10	0.2	$\sim$1.9	5.0	2.8×10^8	17.31	8.05 ± 0.09	8.18 ± 0.03	(1)
SN 2007bi	0.127	-16.05 ± 0.10	0	$\sim$2.1	0.01	1.4×10^8	0.07	–	8.14/8.50	(2)
PS1-11ap	0.524	-17.79 ± 0.32	0	$\sim$1.5	0.47 ± 0.12	1.5×10^9	0.31	–	8.1/8.5	(3)

(1) This work; (2) this work and Young et al. (2010); (3) McCrum et al. (2014).

practical problem for detailed studies of both the host galaxy and late evolution of the SN. Disentangling the flux of the SN and that of the host requires deep imaging over a period of several years to be sure that uncontaminated host flux is recovered and can be used as a reliable template to recover the faint and fading SN. High spatial resolution imaging with *HST*, as done by Lunnan et al. (2014), can help resolve the ambiguity. In this paper we demonstrated that it can be done from ground-based imaging, even in the case of a relatively bright, marginally resolved host galaxy with the SN occurring in the core. We demonstrated recovery of the SN flux when it is around 1–2 per cent of the host galaxy light.

The data presented here extend the light curve of PTF12dam out to +400 d after peak allowing further testing of the three competing models for SLSNe Ic. The new data points indicate that PTF12dam declines faster than expected from the study of the first 200 d by Nicholl et al. (2013). We find that published pair-instability models cannot quantitatively fit full the bolometric light curve, as originally suggested in Nicholl et al. (2013). The magnetar model is still viable, but the opacity in the ejecta needs to be lowered to $\kappa_\gamma \simeq 0.01$ cm^2 g^{-1}. This is physically plausible if the high-energy radiation that provides the power is dominated by high-energy gamma-rays produced via pair-production. This is an area that should be explored further with more detailed theoretical treatment. Finally, the model of interaction of the ejecta with a dense CSM which thermalizes the kinetic energy and powers the bright event fits the full bolometric light curve quite well. However as discussed in Nicholl et al. (2014), the configuration of a 13-$M_\odot$ CSM shell (which is H and He free) and 29 $M_\odot$ of ejecta is hard to reconcile with plausible stellar progenitors. Wherever the extra energy comes from to power these types of SLSNe, the progenitors are almost certainly carbon–oxygen stars in very metal poor galaxies.

We derive a reliable value for the metallicity of the galaxy of $12 + \log(\mathrm{O/H}) = 8.05 \pm 0.09$ dex from the direct, electron temperature method (via detection of the weak [O III] λ4363 line). This is the fourth measurement of oxygen abundance in a SLSN host with this T_e method and all values are between 7.5 and 8.0 dex. This supports the previous suggestions of Chen et al. (2013) and Lunnan et al. (2014) that low metallicity is a requirement to produce the stellar progenitor systems that give rise to these peculiar SNe. Their rarity may be explained by this requirement to be formed at very low metallicity.

ACKNOWLEDGEMENTS

The research leading to these results has received funding from the European Research Council under the European Union's Seventh Framework Programme (FP7/2007-2013)/ERC Grant agreement no. [291222] (PI: S. J. Smartt). T-WC thanks Daniel Kasen for the PISN models, and expresses appreciation for Yen-Chen Pan, Kai-Lung Sun, Meng-Chun Tsai, Chorng-Yuan Hwang, Max Pettini, Mark Sullivan, Gary J. Ferland, Edward Schlafly and David R. Young for their useful advice. After the submission to the archive, this article has benefited greatly from the helpful feedback from the referee and Giorgos Leloudas, Avishay Gal-Yam, Alan Fitzsimmons, Michel Dennefeld and Paul Vreeswijk. RPK and FB acknowledge support by the National Science Foundation under grant AST-100878798. NE-R acknowledges the support from the European Union Seventh Framework Programme (FP7/2007-2013) under grant agreement no. 267251 Astronomy Fellowships in Italy (AstroFIt). MF is supported by the European Union FP7 programme through ERC grant no. 320360.

This work is based on observations collected at the WHT, operated on the island of La Palma by the Isaac Newton Group of Telescope; the LT, which is operated by Liverpool John Moores University in the Spanish Observatorio del Roque de los Muchachos of the Instituto de Astrofisica de Canarias with financial support from the UK Science and Technology Facilities Council; the GTC, installed in the Spanish Observatorio del Roque de los Muchachos of the Instituto de Astrofísica de Canarias, in the island of La Palma; the NOT, operated by the Nordic Optical Telescope Scientific Association at the Observatorio del Roque de los Muchachos, La Palma, Spain, of the Instituto de Astrofisica de Canarias.

REFERENCES

Ahn C. P. et al., 2012, ApJS, 203, 21
Amorín R. O., Pérez-Montero E., Vílchez J. M., 2010, ApJ, 715, L128
Amorín R., Pérez-Montero E., Vílchez J. M., Papaderos P., 2012, ApJ, 749, 185
Amorín R. et al., 2014, A&A, 568, L8
Arnett W. D., 1982, ApJ, 253, 785
Asplund M., Grevesse N., Sauval A. J., Scott P., 2009, ARA&A, 47, 481
Baldwin J. A., Phillips M. M., Terlevich R., 1981, PASP, 93, 5
Benetti S. et al., 2014, MNRAS, 441, 289
Berg D. A. et al., 2012, ApJ, 754, 98
Berger E. et al., 2012, ApJ, 755, L29
Blanton M. R., Roweis S., 2007, AJ, 133, 734
Botticella M. T., Smartt S. J., Kennicutt R. C., Cappellaro E., Sereno M., Lee J. C., 2012, A&A, 537, A132
Bouchet P., Slezak E., Le Bertre T., Moneti A., Manfroid J., 1989, A&AS, 80, 379
Bresolin F., 2011, ApJ, 729, 56
Brinchmann J., Kunth D., Durret F., 2008, A&A, 485, 657
Bruzual G., Charlot S., 2003, MNRAS, 344, 1000
Calzetti D., Armus L., Bohlin R. C., Kinney A. L., Koornneef J., Storchi-Bergmann T., 2000, ApJ, 533, 682
Cardamone C. et al., 2009, MNRAS, 399, 1191
Cardelli J. A., Clayton G. C., Mathis J. S., 1989, ApJ, 345, 245
Chatzopoulos E., Wheeler J. C., Vinko J., 2012, ApJ, 746, 121
Chen T.-W. et al., 2013, ApJ, 763, L28
Chevalier R. A., Irwin C. M., 2011, ApJ, 729, L6
Chilingarian I. V., Zolotukhin I. Y., 2012, MNRAS, 419, 1727
Chilingarian I. V., Melchior A.-L., Zolotukhin I. Y., 2010, MNRAS, 405, 1409
Chomiuk L. et al., 2011, ApJ, 743, 114
da Cunha E., Charlot S., Elbaz D., 2008, MNRAS, 388, 1595

Dessart L., Hillier D. J., Waldman R., Livne E., Blondin S., 2012, MNRAS, 426, L76
Dexter J., Kasen D., 2013, ApJ, 772, 30
Ergon M. et al., 2014, A&A, 562, A17
Gal-Yam A., 2012, Science, 337, 927
Gal-Yam A. et al., 2009, Nature, 462, 624
Gallazzi A., Charlot S., Brinchmann J., White S. D. M., Tremonti C. A., 2005, MNRAS, 362, 41
Garnett D. R., 1992, AJ, 103, 1330
Gonzalez-Delgado R. M. et al., 1994, ApJ, 437, 239
Guseva N. G., Papaderos P., Meyer H. T., Izotov Y. I., Fricke K. J., 2009, A&A, 505, 63
Hammer F., Flores H., Schaerer D., Dessauges-Zavadsky M., Le Floc'h E., Puech M., 2006, A&A, 454, 103
Hamuy M., Suntzeff N. B., Gonzalez R., Martin G., 1988, AJ, 95, 63
Heger A., Woosley S. E., 2002, ApJ, 567, 532
Heger A., Fryer C. L., Woosley S. E., Langer N., Hartmann D. H., 2003, ApJ, 591, 288
Hoyos C., Koo D. C., Phillips A. C., Willmer C. N. A., Guhathakurta P., 2005, ApJ, 635, L21
Inserra C., Smartt S. J., 2014, ApJ, 796, 87
Inserra C. et al., 2013, ApJ, 770, 128
Izotov Y. I., Stasińska G., Meynet G., Guseva N. G., Thuan T. X., 2006, A&A, 448, 955
Izotov Y. I., Guseva N. G., Thuan T. X., 2011, ApJ, 728, 161
Kasen D., Bildsten L., 2010, ApJ, 717, 245
Kasen D., Woosley S. E., Heger A., 2011, ApJ, 734, 102
Kelly P. L., Filippenko A. V., Modjaz M., Kocevski D., 2014, ApJ, 789, 23
Kennicutt R. C., Jr, 1998, ARA&A, 36, 189
Kewley L. J., Dopita M. A., 2002, ApJS, 142, 35
Kewley L. J., Brown W. R., Geller M. J., Kenyon S. J., Kurtz M. J., 2007, AJ, 133, 882
Kobulnicky H. A., Kennicutt R. C., Jr, Pizagno J. L., 1999, ApJ, 514, 544
Kotera K., Phinney E. S., Olinto A. V., 2013, MNRAS, 432, 3228
Kozyreva A., Blinnikov S., Langer N., Yoon S.-C., 2014, A&A, 565, A70
Kriek M., van Dokkum P. G., Labbé I., Franx M., Illingworth G. D., Marchesini D., Quadri R. F., 2009, ApJ, 700, 221
Kudritzki R.-P., Urbaneja M. A., Gazak Z., Bresolin F., Przybilla N., Gieren W., Pietrzyński G., 2012, ApJ, 747, 15
Kuncarayakti H. et al., 2013, AJ, 146, 30
Kunth D., Sargent W. L. W., 1981, A&A, 101, L5
Le Borgne D., Rocca-Volmerange B., 2002, A&A, 386, 446
Lee J. C., Salzer J. J., Melbourne J., 2004, ApJ, 616, 752
Lee H., Skillman E. D., Cannon J. M., Jackson D. C., Gehrz R. D., Polomski E. F., Woodward C. E., 2006, ApJ, 647, 970
Leitherer C. et al., 1999, ApJS, 123, 3
Leloudas G. et al., 2015, MNRAS, 449, 917
Liang Y. C., Hammer F., Yin S. Y., Flores H., Rodrigues M., Yang Y. B., 2007, A&A, 473, 411
Longair M. S., 1992, High Energy Astrophysics. Vol. 1: Particles, Photons and their Detection. Cambridge Univ. Press, Cambridge
Lunnan R. et al., 2013, ApJ, 771, 97
Lunnan R. et al., 2014, ApJ, 787, 138
Lunnan R. et al., 2015, ApJ, 804, 90
McCrum M. et al., 2014, MNRAS, 437, 656
McGaugh S. S., 1991, ApJ, 380, 140 (M91)
Maraston C., 2005, MNRAS, 362, 799
Mendoza C., Zeippen C. J., 1982, MNRAS, 199, 1025
Metzger B. D., Vurm I., Hascoët R., Beloborodov A. M., 2014, MNRAS, 437, 703
Modjaz M. et al., 2008, AJ, 135, 1136
Neill J. D. et al., 2011, ApJ, 727, 15
Nicholl M. et al., 2013, Nature, 502, 346
Nicholl M. et al., 2014, MNRAS, 444, 2096
Osterbrock D. E., 1989, Astrophysics of Gaseous Nebulae and Active Galactic Nuclei. University Science Books, Mill Valley, CA
Osterbrock D. E., Ferland G. J., 2006, Astrophysics of Gaseous Nebulae and Active Galactic Nuclei, 2nd edn. University Science Books, Mill Valley, CA
Pastorello A. et al., 2010, ApJ, 724, L16
Pettini M., Pagel B. E. J., 2004, MNRAS, 348, L59 (PP04)
Pilyugin L. S., Thuan T. X., Vílchez J. M., 2003, A&A, 397, 487
Quimby R. M., Aldering G., Wheeler J. C., Höflich P., Akerlof C. W., Rykoff E. S., 2007, ApJ, 668, L99
Quimby R. M. et al., 2011, Nature, 474, 487
Quimby R. M., Yuan F., Akerlof C., Wheeler J. C., 2013, MNRAS, 431, 912
Richer M. G., McCall M. L., 1995, ApJ, 445, 642
Savaglio S., Glazebrook K., Le Borgne D., 2009, ApJ, 691, 182
Schlafly E. F., Finkbeiner D. P., 2011, ApJ, 737, 103
Schlegel D. J., Finkbeiner D. P., Davis M., 1998, ApJ, 500, 525
Skillman E. D., Kennicutt R. C., Hodge P. W., 1989, ApJ, 347, 875
Smith N., McCray R., 2007, ApJ, 671, L17
Smith N., Chornock R., Li W., Ganeshalingam M., Silverman J. M., Foley R. J., Filippenko A. V., Barth A. J., 2008, ApJ, 686, 467
Starling R. L. C. et al., 2011, MNRAS, 411, 2792
Steele I. A. et al., 2004, in Oschmann J. M., Jr, ed., Proc. SPIE Conf. Ser. Vol. 5489, Ground-based Telescopes. SPIE, Bellingham, p. 679
Stoll R., Prieto J. L., Stanek K. Z., Pogge R. W., Szczygieł D. M., Pojmański G., Antognini J., Yan H., 2011, ApJ, 730, 34
Svensson K. M., Levan A. J., Tanvir N. R., Fruchter A. S., Strolger L.-G., 2010, MNRAS, 405, 57
Thöne C. C., de Ugarte Postigo A., García-Benito R., Leloudas G., Schulze S., Amorín R., 2014, preprint (arXiv:1411.1104)
Vreeswijk P. M. et al., 2014, ApJ, 797, 24
Woosley S. E., 2010, ApJ, 719, L204
Woosley S. E., Blinnikov S., Heger A., 2007, Nature, 450, 390
Wright E. L., 2006, PASP, 118, 1711
Wright E. L. et al., 2010, AJ, 140, 1868
Yaron O., Gal-Yam A., 2012, PASP, 124, 668
Young D. R. et al., 2010, A&A, 512, A70

This paper has been typeset from a TEX/LATEX file prepared by the author.